M. Sc. Thesis

Geophysics

Turbulence measurements in the water-side surface boundary layer of a boreal lake

Aki Vähä

2018

Supervisor: Ivan Mammarella

Reviewers: Petteri Uotila, Timo Vesala

UNIVERSITY OF HELSINKI

INSTITUTE OF ATMOSPHERIC RESEARCH INAR

PL 64 (Gustaf Hällströmin katu 2)

00014 University of Helsinki

HELSINGIN YLIOPISTO — HELSINGFORS UNIVERSITET — UNIVERSITY OF HELSINKI

Tiedekunta/Osasto — Fakultet/Sektion — Faculty	Osasto — Avdelning — Department
Matemaattis-luonnontieteellinen tiedekunta	Ilmakehätieteiden keskus INAR

Tekijä — Författare — Author
Aki Vähä

Työn nimi — Arbetets titel — Title
Turbulence measurements in the water-side surface boundary layer of a boreal lake

Oppiaine — Läroämne — Subject
Geofysiikka

Työn laji — Arbetets art — Level	Aika — Datum — Month and year	Sivumäärä — Sidoantal — Number of pages
Pro gradu -tutkielma	Lokakuu 2018	59

Tiivistelmä — Referat — Abstract

Havumetsävyöhykkeet järvet ovat tärkeässä asemassa maailmanlaajuisessa hiilen kierrossa. Järvet kuljettavat ja varastoivat hiiltä ja vaihtavat sitä ilmakehän kanssa. Koska turbulenssi on merkittävin prosessi, joka kuljettaa aineita vedessä ja ilmassa, järvissä tapahtuva turbulenttinen kuljetus on erityisen mielenkiinnon kohde.

Tämä tutkielma keskittyy pinnan rajakerroksen turbulenssiin Kuivajärvessä, joka sijaitsee Länsi-Suomessa. Syyskuussa 2014 Kuivajärvellä järjestettiin 16 päivän mittauskampanja. Sen aikana tehtiin korkeataajuuksisia veden nopeusmittauksia akustisella Doppler-velosimetrillä (ADV). Kampanjanaikainen sääpakote jakautui kahteen osaan: suhteellisen tyyneen ja lämpimään kauteen ensimmäisten 13 päivän aikana sekä kylmään ja tuuliseen kauteen viimeisten kolmen päivän aikana. Sama kaksijakoisuus erottui mitatussa nopeudessa ja lasketuissa turbulenssiparametreissä.

Veden kitkanopeuden arviot olivat $3 \cdot 10^{-4} \ldots 2 \cdot 10^{-2}$ m s^{-1}, kun tuulennopeus oli alhainen, ja $2 \cdot 10^{-3} \ldots 5 \cdot 10^{-2}$ m s^{-1} kovien tuulten aikaan. Alhaisen tuulennopeuden vallitessa veden kitkanopeus oli yleisesti pienempi kuin skaalattu kitkanopeus ilmassa. Kun tuulennopeus oli suuri, tilanne oli päinvastainen. Yleinen tapa määrittää veden kitkanopeus pinnanpäällisistä mittauksista ei ole kaikissa olosuhteissa hyväksyttävä.

Viskoosi dissipaationopeus laskettiin inertiaalisen alialueen menetelmällä sekä neutraalista skaalauksesta. Tuulennopeuden ollessa pieni dissipaationopeuden suuruusluokka-arviot vaihtelivat 10^{-10}:stä 10^{-4}:ään W kg^{-1}. Jaksoissa, joissa tuulennopeus oli suuri, arviot olivat $\sim 10^{-7} \ldots 10^{-3}$ W kg^{-1}. On todennäköistä, että korkeimmat arviot ovat virheellisiä, koska näin korkeita arvoja ei ole mitattu järvissä muualla.

Työssä kokeiltiin yksinkertaistettua turbulenttisen liike-energian yhtälöä, joka sisälsi dissipaationopeuden, väännetuoton sekä nostetuoton. Turbulenssin tuotossa ja dissipaatiossa havaittiin olevan epätasapainon, joka sekin liittyi kahteen sääpakotteeseen. Yhtälöön pitäisi mahdollisesti sisällyttää myös turbulenttiseen kuljetukseen liittyviä termejä.

Mittausten merkittävimmät virhelähteet olivat nopeusaikasarjassa esiintyvä kohina sekä aaltojen vaikutus. Tutkielmassa näytettiin, että kohinanpoisto on oleellinen osa ADV-data-analyysiä. Kohinanpoistomenetelmiä pitää kehittää edelleen samoin kuin dissipaationopeuden laskentamenetelmiä. ADV-laitteen kiinnitystä pitää myös parantaa.

Avainsanat — Nyckelord — Keywords
turbulenssi, rajakerros, akustinen Doppler-velosimetri, kitkanopeus, viskoosi dissipaatio, järvi

Säilytyspaikka — Förvaringsställe — Where deposited
Kumpulan tiedekirjasto

Muita tietoja — övriga uppgifter — Additional information

HELSINGIN YLIOPISTO — HELSINGFORS UNIVERSITET — UNIVERSITY OF HELSINKI

Tiedekunta/Osasto — Fakultet/Sektion — Faculty	Osasto — Avdelning — Department
Faculty of Science	Institute of Atmospheric Research INAR

Tekijä — Författare — Author
Aki Vähä

Työn nimi — Arbetets titel — Title
Turbulence measurements in the water-side surface boundary layer of a boreal lake

Oppiaine — Läroämne — Subject
Geophysics

Työn laji — Arbetets art — Level	Aika — Datum — Month and year	Sivumäärä — Sidoantal — Number of pages
M.Sc. Thesis	October 2018	59

Tiivistelmä — Referat — Abstract

Lakes in the boreal region hold a significant importance in the global carbon cycle. They transport and store carbon and exchange it with the atmosphere. As turbulent transport is the most important process in transporting substances in water and air, special weight has been laid on studying turbulent processes in lakes.

This work concentrates on turbulence in the surface boundary layer of Lake Kuivajärvi in Western Finland. A 16-day measurement campaign was carried out in Kuivajärvi in September 2014. An acoustic Doppler velocimeter (ADV) was used for high-frequency velocity measurements. The meteorological forcing had two distinct regimes during the campaign: a relatively calm and warm period during the first 13 days and a cold and windy period during the last three days. The two regimes were visible in the measured velocity as well as in the calculated turbulence parameters.

The friction velocity in water was estimated to be $3 \cdot 10^{-4} \ldots 2 \cdot 10^{-2}$ m s^{-1} during low winds and $2 \cdot 10^{-3} \ldots 5 \cdot 10^{-2}$ m s^{-1} during high winds. In the low-wind regime, the friction velocity in water was generally smaller than the scaled friction velocity in air. In the high-wind regime, the situation was opposite. The common practice of estimating the water-side friction velocity from above-surface measurements isn't justified in all conditions.

The viscous dissipation rate was calculated using the inertial subrange method and the neutral scaling. Dissipation rate estimates were from $\sim 10^{-10}$ to 10^{-4} W kg^{-1} during the low-wind regime. During the high-wind regime, the estimates ranged from $\sim 10^{-7}$ to 10^{-3} W kg^{-1}. It is likely that the highest dissipation rate estimates were erroneous as such high values have not been reported elsewhere in lakes.

A simplified turbulent kinetic energy equation with dissipation rate, shear production and buoyancy production was tested. There was an imbalance of turbulence production and dissipation that was also related to the two meteorological regimes. Whether the equation should also include turbulent transport terms is an open question.

The most important sources for errors were noise in the velocity time series and the effect of waves. It was shown that noise removal is an essential part of the ADV data analysis, however, noise-removal methods and methods for calculating the dissipation rate should be developed further. The installment of the ADV instrument should also be improved.

Avainsanat — Nyckelord — Keywords
turbulence, boundary layer, acoustic Doppler velocimeter, friction velocity, viscous dissipation, lake

Säilytyspaikka — Förvaringsställe — Where deposited
Kumpula Campus library

Muita tietoja — övriga uppgifter — Additional information

Contents

1 Introduction **3**

2 Theory **6**

2.1 Turbulence 6

2.1.1 Reynolds averaging and fluxes 6

2.1.2 Turbulent kinetic energy 8

2.1.3 Friction velocity 9

2.2 Turbulence spectrum 11

2.2.1 Power spectrum and cross spectrum 11

2.2.2 Kolmogorov spectrum and inertial subrange 12

2.2.3 Viscous dissipation of turbulent kinetic energy 14

2.3 Surface boundary layer 15

3 Instruments, data and methods **17**

3.1 Site 17

3.2 Instruments and data 19

3.2.1 Acoustic Doppler velocimeter 19

3.2.2 Other instruments 23

3.3 Methods 24

3.3.1 Properties of water 24

3.3.2 ADV data processing methods 24

4 Results and discussion **31**

4.1 Meteorological conditions and water temperature profiles 31

4.2 Velocity time series 35

4.3 Power spectra, cospectra and turbulence parameters 39

4.3.1 Power spectra and cospectra 39

4.3.2 Friction velocity 43

4.3.3 Viscous dissipation 44

4.3.4 Noise removal 48

4.3.5 Turbulent kinetic energy 51

5 Conclusions **54**

Chapter 1

Introduction

Lakes in the boreal region have a significant impact on the local climate and biogeochemical cycles. In recent years, it has been understood that especially small lakes are more numerous and hold a larger total area than what has been thought earlier (Downing et al., 2006; Verpoorter et al., 2014). Most inland waters are found in the boreal and arctic regions (Verpoorter et al., 2014) where they can cover a significant portion of the total inland area: for example, 9.9% of Finland (Tikkanen, 2002).

Lakes hold a significant importance in the global carbon cycle as they transport and store carbon and exchange it with the atmosphere. The net annual carbon dioxide (CO_2) flux from natural lakes into the atmosphere is about 0.11 Pg C y^{-1} (Cole et al., 2007). Due to their relatively small size, lakes are particularly susceptible to a warming climate and have already shown signs of a significant warming (O'Reilly et al., 2015).

As turbulent transport is the most important process in transporting substances in water and air, special weight has been laid on studying the turbulent processes in lakes. Most of the theory about water-side surface boundary layer (SBL) was originally developed for the oceanic surface layer but the theory can be applied to lakes as well. Early studies include e.g. Dillon et al. (1981), who studied vertical profiles of the dissipation of turbulence in a reservoir, and Lombardo and Gregg (1989), who studied the convective processes and the viscous and

thermal dissipation in the oceanic SBL. Imberger (1985) and Kocsis et al. (1999) studied the structure and diurnal behaviour of the SBL in a lake and also the dissipation of turbulence using a microstructure profiler.

More modern studies have often expanded the view of turbulence into the exchange of gasses at the air–water interface. Vachon et al. (2010) utilised acoustic Doppler velocimetry to quantify turbulence and determined gas transfer coefficients at the surface. Czikowsky et al. (2018) measured turbulence and CO_2 with a microstructure profiler and in a lake to determine the CO_2 flux at the interface. Special weight was laid on the meteorological forcing on the turbulence and the flux. Tedford et al. (2014) studied turbulent processes in the SBL of a lake during the autumn cooling.

This work concentrates on studying the turbulence in the surface boundary layer of Lake Kuivajärvi in Finland. Kuivajärvi has been the subject of extensive earlier research. Earlier works include e.g. Heiskanen et al. (2014) who measured and modelled gas transfer velocities between the lake and the atmosphere, and Mammarella et al. (2015) who studied carbon dioxide and energy fluxes using the eddy covariance technique.

A measurement campaign was conducted in Kuivajärvi in September 2014. During the campaign, eddy covariance and floating chamber measurements were conducted as well as acoustic Doppler velocimeter and microstructure profiler measurements. Results from eddy covariance and floating chamber measurements have been used by Erkkilä et al. (2018), who calculated gas transfer velocities from the lake to the atmosphere for methane and carbon dioxide.

The purpose of this study is

1. to test the installment of the ADV by analysing the data,

2. to see how different noise-removal methods can be applied to this data and how they compare to each other, and

3. to see whether a simplified turbulent kinetic energy balance equation can be applied to the data.

The first and second goal are related to technical and computational questions about improving the data quality. The third goal, if fulfilled, would enable a much deeper analysis of the turbulent quantities than what is within the scope of this study.

The thesis is divided into five sections. In section 'Theory', the basic theory of turbulence and spectral analysis is presented. In section 'Instruments, data and methods', the principle of acoustic Doppler velocimetry is introduced as well as its data processing methods. Most weight is laid on the noise-removal processes. Also other instruments are presented. Section 'Results and discussion' shows the most important results from the campaign and they are discussed and compared to results from other similar studies. Finally, the most important results are presented in section 'Conclusions'.

Chapter 2

Theory

2.1 Turbulence

2.1.1 Reynolds averaging and fluxes

Any time-dependent variable $x = x(t)$ can be decomposed into average and deviatoric component

$$x = \overline{x} + x', \tag{2.1}$$

where the overbar denotes the time average and x' is the deviation from the average. This is known as the Reynolds decomposition, where time averaging is defined as

$$\overline{x} = \frac{1}{T}\int_{t}^{t+T} x(t')\mathrm{d}t', \tag{2.2}$$

where T is the averaging time. (Tennekes and Lumley, 1972)

In the case of two time-dependent arbitrary variables x and y, the mean of their product is

$$\overline{xy} = \overline{x}\,\overline{y} + \overline{x'y'}. \tag{2.3}$$

Henceforth, the velocity vector $\vec{U}$ will be divided into orthogonal components so that

$$\vec{U} = u\hat{\imath} + v\hat{\jmath} + w\hat{k}. \tag{2.4}$$

Here, the w component is the vertical velocity and u and v lie in the horizontal direction. The directions of u and v can be arbitrary, but the common practise that is also used in this work, is that the direction of the mean flow is along the u component. In the case of the other variable in equation (2.3) being the vertical velocity w and also assuming that the mean vertical velocity $\overline{w}$ is zero, we get the vertical turbulent flux of the arbitrary variable x:

$$F_x = \overline{w'x'}. \tag{2.5}$$

It is also assumed that the flow doesn't experience any horizontal divergence of convergence. (Tennekes and Lumley, 1972)

Using equation (2.5), we can define vertical energy fluxes and the momentum flux. The vertical flux of the momentum ρu, or the Reynolds shear stress in the direction of u, is

$$\tau_{xz} = -\rho\overline{u'w'} \tag{2.6}$$

where ρ is the mass density of the fluid. Similarly in the direction of v, the shear stress is

$$\tau_{yz} = -\rho\overline{v'w'}. \tag{2.7}$$

The total shear stress, or the total vertical momentum flux, is

$$\tau = \left[\tau_{xz}^2 + \tau_{yz}^2\right]^{1/2} = \rho\left(\overline{u'w'}^2 + \overline{v'w'}^2\right)^{1/2}. \tag{2.8}$$

Both the u and v velocity components contribute to the vertical flux. However, if the u component is aligned with the mean flow, the $\overline{v'w'}$ term becomes 0 because then $\overline{v'} = 0$. The sensible heat flux is

$$H = \rho c_p\overline{w'\theta'}, \tag{2.9}$$

where c_p is the specific heat capacity of the fluid and θ is the potential temperature. The latent heat flux is

$$LE = \rho L\overline{q'w'}, \tag{2.10}$$

where L is the latent heat of evaporation and q is the mixing ratio of water vapour in air.

2.1.2 Turbulent kinetic energy

Turbulent kinetic energy (TKE) per unit mass is

$$E_{\mathrm{k}} = \frac{1}{2}\left(\overline{u'^2} + \overline{v'^2} + \overline{w'^2}\right). \tag{2.11}$$

The three terms in the parenthesis are the variances of the velocity components. The mean kinetic energy, $\frac{1}{2}\left(\overline{u}^2 + \overline{v}^2 + \overline{w}^2\right)$, is the energy pertaining to the mean flow. The turbulent kinetic energy is then the energy that the turbulent eddies possess (Kaimal and Finnigan, 1994).

Turbulent kinetic energy equation describes how the TKE changes with respect to time. The equation can be written as

$$\frac{\mathrm{D}E_{\mathrm{k}}}{\mathrm{D}t} = \frac{\partial E_{\mathrm{k}}}{\partial t} = \underbrace{-\overline{u'w'}\left(\frac{\partial \overline{u}}{\partial z}\right)}_{\mathrm{I}} \underbrace{+\frac{g}{\overline{\theta}}\overline{w'\theta'}}_{\mathrm{II}} \underbrace{-\frac{1}{\rho}\frac{\partial}{\partial z}\overline{w'p'}}_{\mathrm{III}} \underbrace{-\frac{\partial}{\partial z}\overline{E_{\mathrm{k}}w'}}_{\mathrm{IV}} \underbrace{-\varepsilon}_{\mathrm{V}}, \tag{2.12}$$

where g is the gravitational acceleration and p is the pressure (Kaimal and Finnigan, 1994).

Term I in (2.12) is the production of turbulence caused by velocity shear. Term II is the buoyancy flux. The temperature structure in the point in question can either suppress or enhance turbulence, depending on whether the situation is stable or unstable. Term III is the pressure transport term. Term IV is the vertical transport of turbulence caused by the turbulence itself. Term V is the dissipation of turbulence by viscosity of the fluid into heat. When the TKE equation is written in this form, it is assumed that there is no horizontal advection of turbulence, which can also be seen from the change of the total time derivative into a partial derivative (Kaimal and Finnigan, 1994).

Terms I and V will be discussed later. Term II, the buoyancy flux which will be further on denoted as J_{B}, is the effect of stability on the turbulence. When positive, the term is the production of turbulence by convection. When negative, it is the suppression of turbulence by buoyancy. The buoyancy flux at the surface can be estimated as

$$J_{\mathrm{B}} = \frac{g\alpha_{\mathrm{w}}H_*}{c_{\mathrm{p,w}}\rho_{\mathrm{w}}}, \tag{2.13}$$

where $\alpha_{\mathrm{w}} = \frac{1}{V}\left(\frac{\partial V}{\partial T}\right)_{\mathrm{p}}$ is the thermal expansion coefficient of water, $c_{\mathrm{p,w}}$ is the specific heat capacity of water and ρ_{w} is the density of water (Tedford et al., 2014). The term H_* is the total heat flux into the surface and is defined as

$$H_* = SW_{\downarrow} - SW_{\uparrow} + LW_{\downarrow} - LW_{\uparrow} + H + LE, \tag{2.14}$$

where SW refers to shortwave and LW to longwave radiation. Arrows down represent radiation to the surface and arrows up radiation from the surface. The signs of the fluxes are chosen to be positive when the flux is into the surface. The term $SW_{\downarrow}$ should include only the part of the downward shortwave radiation that is absorbed in the mixing layer.

Buoyancy flux that is calculated from surface variables in (2.13) is defined at the surface. The water-side measurements in this work were not done directly at the surface but 29 cm below it. We will still use the surface measurements because no better estimate for the fluxes in the water column are available.

Terms III and IV, the transport terms in (2.12), are left out completely in this work. Term III is difficult to estimate without a high-frequency time series of pressure. The magnitude of the term is also likely to be close to 0 because the measurements are made at a constant depth and p' is therefore small. The advection of turbulence can be left out on the assumption that the boundary layer is horizontally homogeneous.

2.1.3 Friction velocity

The friction velocity u_* is a measure of mechanically produced turbulence. From the turbulent shear stress τ in equation (2.8), friction velocity is defined as

$$u_* = \left(\frac{\tau}{\rho}\right)^{1/2} = \left(\overline{u'w'}\right)^{1/2}, \tag{2.15}$$

(Weber, 1999).

At the air–water interface, it is assumed that the shear stresses acting on the interface from the air and water side are equal:

$$\tau_{\mathrm{w}} = \tau_{\mathrm{a}}, \tag{2.16}$$

or, using the definition of the friction velocity,

$$\rho_{\mathrm{w}} u_{*,\mathrm{w}}^2 = \rho_{\mathrm{a}} u_{*,\mathrm{a}}^2, \tag{2.17}$$

where the subscripts w and a refer to quantities for water and air, respectively. If the only measurements of the friction velocity are from above surface, equation (2.17) can be solved for $u_{*,\mathrm{w}}$ to get the scaled friction velocity in water:

$$u_{*,\mathrm{w}} = \sqrt{\frac{\rho_{\mathrm{a}}}{\rho_{\mathrm{w}}}} u_{*,\mathrm{a}}. \tag{2.18}$$

The friction velocity is a scaling parameter for vertical flow profiles. In the case of a neutrally stratified boundary layer, the gradient of the mean flow is inversely proportional to the distance z from the interface, as

$$\frac{\partial U}{\partial z} = \frac{u_*}{kz}, \tag{2.19}$$

where $k = 0.40$ is von Kármán's constant (Kaimal and Finnigan, 1994).

As was discussed earlier, the only processes that contribute to the production of turbulence in the simplified model are shear and buoyancy. It is also assumed that the system is in steady state, that is, $\frac{\partial E_{\mathrm{k}}}{\partial t} = 0$. By using the definition of friction velocity, equation (2.12) becomes

$$0 = P_{\mathrm{S}} + J_{\mathrm{B}} - \varepsilon = -\overline{u'w'} \left(\frac{\partial \bar{u}}{\partial z} \right) + J_{\mathrm{B}} - \varepsilon \tag{2.20}$$

where P_{S} is now the shear production.

Assuming a neutral stratification ($\frac{g}{\theta}\overline{w'\theta'} = 0$), in which case the buoyancy procuction term equals zero, equation (2.20) reduces to

$$-\overline{u'w'} \left(\frac{\partial \bar{u}}{\partial z} \right) = \frac{u_*^3}{kz} = \varepsilon. \tag{2.21}$$

This is the well-known equilibrium assumption used often in the surface layer. The neutral friction velocity is then

$$u_* = (\varepsilon k z)^{1/3}. \tag{2.22}$$

2.2 Turbulence spectrum

2.2.1 Power spectrum and cross spectrum

The power spectral density, or power spectrum as it is often referred to, is defined as the Fourier transform of the autocovariance function. For a ergodic, stationary time series $g(t)$, the autocovariance as a function of the time lag τ is

$$R_g(\tau) = \lim_{T\to\infty} \frac{1}{T} \int_0^T g(t+\tau)g(t)\mathrm{d}t. \tag{2.23}$$

The power spectrum of $g(t)$ is then

$$S_g(\omega) = \frac{1}{2\pi} \int_{-\infty}^{+\infty} R_g(\tau)e^{-i\omega\tau}\mathrm{d}\tau, \tag{2.24}$$

where ω is the angular frequency of a specific wave component (Bendat and Piersol, 2011).

Similarly, for two time series $g(t)$ and $h(t)$, the cross covariance function is

$$R_{gh}(\tau) = \lim_{T\to\infty} \frac{1}{T} \int_0^T g(t+\tau)h(t)\mathrm{d}t \tag{2.25}$$

and the cross-spectral density or cross spectrum is

$$S_{gh}(\omega) = \frac{1}{2\pi} \int_{-\infty}^{+\infty} R_{gh}(\tau)e^{-i\omega\tau}\mathrm{d}\tau. \tag{2.26}$$

Usually only the positive frequencies are used, in which case a one-sided cross-spectrum is defined as

$$S'_{gh} = 2S_{gh} = C_{gh} - iQ_{gh}, \tag{2.27}$$

when $0 < \omega < \infty$. The functions C_{gh} and Q_{gh} are the co-spectrum and quadrature spectrum, respectively (Bendat and Piersol, 2011).

From here on, the prime in equation (2.27) will be dropped and only one-sided power spectra are used. The spectral density functions S_{gg} are real-valued. In contrast, the functions S_{gh} are complex-valued, as can be seen from equation (2.27). The co-spectral density C_{gh} is of most

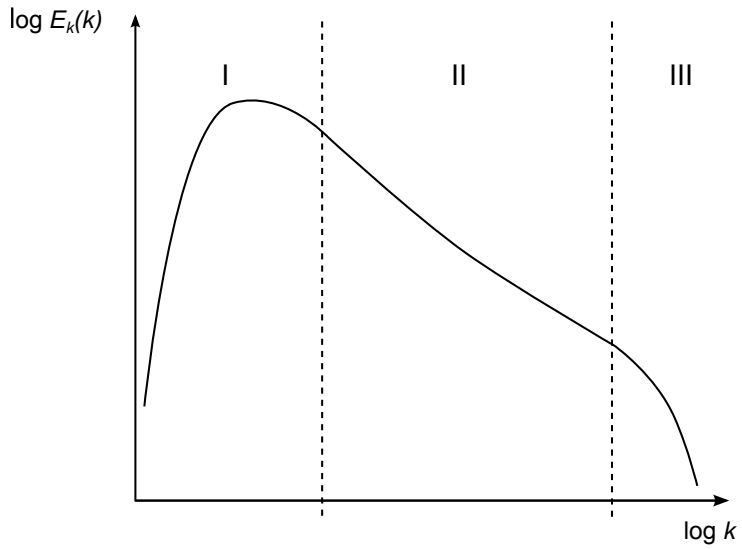

Figure 2.1: A schematic drawing of the TKE spectrum as a function of the wavenumber κ. The spectrum is divided into three ranges: the energy-containing range (I), the inertial subrange (II) and the dissipation range (III).

value for this work as it shows the spectral behaviour of the covariance of two variables. As was shown with equation (2.5) in section 2.1.1, the covariance is the flux.

The area of a power spectrum equals, when correctly scaled, the variance of the time series. Likewise, the integral of a cospectrum equals the covariance of the two variables in question.

2.2.2 Kolmogorov spectrum and inertial subrange

A sketch of the turbulent kinetic energy as a function of wavenumber $\kappa = 2\pi/\lambda$ (λ is the wavelength) is shown in figure 2.1. Turbulent kinetic energy is fed into the system at the energy-containing range. These are the wavenumbers where the processes producing TKE, such as wind-generated surface waves, work. The characteristic length scale at this range is the Eulerian integral length scale

$$\Lambda = \frac{U}{\sigma_u^2} \int_0^\infty R_u(\tau) \mathrm{d}\tau, \tag{2.28}$$

where σ^2 is the variance, R_u is the autocovariance function of the u velocity component and U is the mean velocity (Kaimal and Finnigan, 1994). The definition of U in this work is

$$U = \frac{1}{N} \sum_{i=1}^{N} \sqrt{u_i^2 + v_i^2 + w_i^2} \tag{2.29}$$

where N is the length of the data record.

Turbulent eddies break up naturally into smaller eddies (smaller wavelengths) or, consequently, into larger wavenumbers. The energy that the turbulent eddies possess cascades therefore towards larger wavenumbers. In the inertial subrange, no turbulent kinetic energy is fed into the system or dissipated out of it but rather the turbulent energy "moves" through this range towards larger wavenumbers. At the dissipation range, the eddies have become so small that viscous forces dominate over inertial motion. Turbulent motion is dissipated into heat. The characteristic length scale here is the Kolmogorov length scale

$$\eta = \left(\frac{\nu^3}{\varepsilon} \right)^{1/4}, \tag{2.30}$$

where ν is the kinematic viscosity of the fluid (Thorpe, 2007).

As no kinetic energy is produced or dissipated at the inertial subrange, the rate of energy moving into the inertial subrange must equal the TKE dissipation rate. Identifying the inertial subrange and calculating the spectrum there gives therefore an estimation of the dissipation rate. At the inertial subrange, the spectrum follows the power law $\kappa^{-5/3}$. The one-dimensional power spectral density $F_i(\kappa)$ of each velocity component $\vec{u}_i$ is of the form

$$F_i(\kappa) = \alpha_i \varepsilon^{2/3} \kappa^{-5/3}. \tag{2.31}$$

The constant α_i depends on the velocity component: for u, the direction of mean advection, $\alpha_1 = 0.52$ and for v and w, $\alpha_2 = \alpha_3 = (4/3)\alpha_1$, assuming local isotropy (Tennekes and Lumley, 1972).

2.2.3 Viscous dissipation of turbulent kinetic energy

Turbulence is often measured as a function of time at a fixed point in space. We therefore need to move from wavenumber spectra $F(\kappa)$ to frequency spectra $S(f)$. An essential assumption in transforming a power spectrum in wavenumber space into frequency space is Taylor's frozen turbulence hypothesis. In this hypothesis, it is assumed that the turbulent motion is slow enough compared to the mean advective flow. Wavenumbers can then be transformed into frequencies if one knows the mean velocity U of the fluid:

$$\kappa = \frac{2\pi}{\lambda} = \frac{2\pi}{UT} = \frac{2\pi f}{U}. \tag{2.32}$$

Using Taylor's hypothesis and $\kappa F(\kappa) = fS(f)$, (2.31) can be written as

$$S(f) = \left(\frac{2\pi}{U}\right)^{-2/3} \alpha_i \varepsilon^{2/3} f^{-5/3} \tag{2.33}$$

and, solving the dissipation rate from this equation, we arrive at

$$\varepsilon = \frac{2\pi}{U} f^{5/2} \left[\frac{S(f)}{\alpha_i}\right]^{3/2} \tag{2.34}$$

(Kaimal and Finnigan, 1994). The viscous dissipation rate ε is a particularly important parameter because it is needed in determining many other parameters such as gas transfer velocities.

If Taylor's hypothesis isn't valid, the turbulent eddies that move past a single measuring point have time to evolve, thus making estimates of turbulent quantities invalid. Turbulent intensity is $I = \sigma_1/U$, where σ_1 is the standard deviation of velocity in the mean direction of advection. When $I \ll 1$, Taylor's hypothesis is considered valid (Bluteau et al., 2011). Even if Taylor's hypothesis doesn't hold, viscous dissipation can be calculated but the estimates have to be improved by implementing a correction method suggested by Hsieh and Katul (1997). The correction function for u direction is

$$F_u(I) = \left(1 + \frac{11}{9} I^2\right) \tag{2.35}$$

and for w direction

$$F_w(I) = \left(1 + \frac{11}{36} I^2\right). \tag{2.36}$$

All estimates of the dissipation rate should then be divided by these values.

2.3 Surface boundary layer

The surface boundary layer (SBL) is the part of the water body from the surface downwards that is affected by the wind shear and buoyancy flux from the surface (Lombardo and Gregg, 1989). In lakes, the SBL reaches from the surface to a depth of a few metres, the thickness of the layer increasing as turbulence increases. The total momentum flux $-\rho u_*^2$ in the SBL is divided into two parts, the momentum flux into the SBL and the momentum flux needed for wave production (Wüest and Lorke, 2003):

$$\tau_{\mathrm{w}} = \tau_{\mathrm{SBL}} + \tau_{\mathrm{wave}}. \tag{2.37}$$

τ_{w} is the water-side momentum flux as in equation 2.16. The effect of waves is restricted to the uppermost part of the SBL, typically less than 1 m. A constant momentum flux, as in equation 2.19, would lead to a logarithmic flow law throughout the SBL (Thorpe, 2007). However, when surface waves are present, the additional stress component τ_{wave} increases the velocity shear $\partial U/\partial z$ in the wave-affected layer close to the surface and consequently the flow profile is nonlogarithmic (Wüest and Lorke, 2003). It is worth noticing that we can only measure the total momentum flux when estimating u_*.

Stability in the SBL is defined as minus the ratio of buoyancy and shear production. From the definition of buoyancy production in equation (2.12) and the definition of shear production in equation (2.21), the stability is

$$\zeta = \frac{z}{L_{\mathrm{MO}}} = -\frac{kz}{u_*^3}\frac{g\overline{w'\theta'}}{\bar{\theta}}, \tag{2.38}$$

where the scaling parameter L is the Monin-Obukhov length

$$L_{\mathrm{MO}} = -\frac{u_*^3\bar{\theta}}{kg\overline{w'\theta'}} \tag{2.39}$$

(Kaimal and Finnigan, 1994).

The stability of the SBL also affects the shear of the flow. It is the surface buoyancy flux J_{B} or essentially the heat flux from or to the surface that dictates the stability. In destabilising

conditions, when $J_{\mathrm{B}} < 0$ and consequently $L_{\mathrm{MO}} < 0$, thermally produced turbulence enhances the vertical momentum transport and the shear of the flow is less than with zero buoyancy flux. In stabilising conditions with $J_{\mathrm{B}} > 0$ and $L_{\mathrm{MO}} > 0$, turbulent energy does work against the buoyancy and a given stress results in a larger shear, compared to the neutral situation (Thorpe, 2007).

The average diurnal cycle of the SBL in water in the summer depends on the wind shear and J_{B}. After sunrise and when the heating commences, L_{MO} is small. The heating causes a thermocline to form close to the surface. The SBL is mostly driven by wind shear but because wind speeds are usually low, the shear is also small. During day, both the heating of the surface as well as wind shear increase. The thickness of the layer that is actively mixed increases. Also L_{MO} deepens and depending on the wind, the mixing is partly or completely wind-driven. During nighttime, the buoyancy flux is negative and causes convection in the SBL (Lombardo and Gregg, 1989; Thorpe, 2007; Tedford et al., 2014).

The development of the SBL can, of course, differ significantly from aforementioned if the wind shear and J_{B} differ from their average behaviour. Also, this average behaviour applies to situations where the temperature of the water is above 4° C such that the thermal expasion coefficient of water is positive. Below 4° C, heating of the surface causes destabilising conditions in the SBL.

Chapter 3

Instruments, data and methods

3.1 Site

Lake Kuivajärvi is an oblong lake situated in western Finland (61° 50' N, 24° 16' E). It is 2.6 km long, some hundreds of metres wide, 141 m above the sea surface and extends in NNW–SSE direction. The maximum depth of the lake is 13.2 m. The surrounding areas are hilly, maximum height differences being about 50 m, and covered with managed boreal forest. The lake water is turbid with the Secchi depth varying between 1.2 and 1.5 m. The Hyytiälä forestry field station of the University of Helsinki as well as the SMEAR II meteorological field station are located close to the lake (Heiskanen et al., 2015; Erkkilä et al., 2018).

The instruments that were used in this work were installed on a raft 3×5 m in size. The raft is anchored approximately in the middle of the southern basin of the lake. Along with the instruments, the raft carries computers and data loggers for the instruments along with water pumps for gas analysers. Power is provided from the shore by a cable. A map of the lake and its surroundings as well as the location of the raft are presented in the map in figure 3.1.

The measuring campaign lasted for 16 days, from the 10th (day of year 253) to the 25th (day 268) of September 2014.

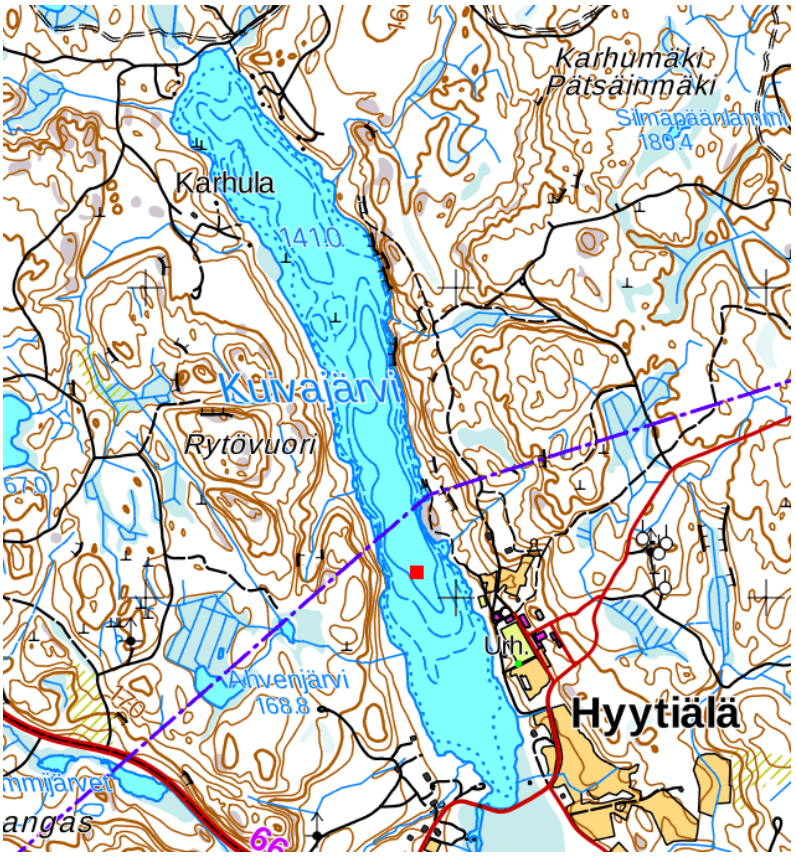

Figure 3.1: A map showing the Lake Kuivajärvi, its surroundings and the bathymetry. The isobaths are 1.5 m (dotted), 3 m and 6 m (dashed), and 10 m (solid). On land, the leading contours (thick brown lines) are at 20 m intervals. The red square in the southern part of the lake marks the location of the raft. The map is from Maanmittauslaitos (2018).

3.2 Instruments and data

3.2.1 Acoustic Doppler velocimeter

An acoustic Doppler velocimeter (ADV) is a sonar that measures the Doppler shift in a scattered ultrasound signal. The sound signal doesn't scatter from water itself but rather from suspended particles in water: plankton or sediments. These particles move with the water and measuring their velocity gives the velocity of water. The quality of ADV measurements depends on the number of scatterers in the measuring volume. Generally in lakes, the amount of scatterers is low and operating an ADV can be difficult (Blanckaert and Lemmin, 2006).

The simplest operation mode of an ADV is such that one signal is transmitted and received before a new one is transmitted. The difference in frequencies of the transmitted and received signals depends on the relative velocity v_{rel} as

$$\Delta f = \frac{2 f v_{\text{rel}}}{c}, \tag{3.1}$$

where f is the frequency of the transmitted pulse and c the speed of sound in the medium. This is known as the Doppler equation. (Blanckaert and Lemmin, 2006)

Usually however, an ADV doesn't measure the frequency of the received signal but rather the phase difference between the transmitted and received pulses. Solving (3.1) for v_{rel} and writing the frequency difference as $\Delta f = \frac{\Delta\phi}{2\pi\Delta t}$, where $\Delta\phi$ is the phase difference and Δt the time between two transmissions or the so-called pulse repeation time, we obtain

$$v_{\text{rel}} = \frac{c\Delta\phi}{4\pi f \Delta t} \tag{3.2}$$

(Lhermitte and Serafin, 1984).

The ADV used in this work is a Nortek Vectrino (Nortek AS, Rud, Norway). It is a four-receiver velocimeter with the transmitter at the centre and the receivers around it. A sketch of the Vectrino measuring head is shown in figure 3.2. The receivers are mounted at 90° angles between each other such that receivers 1 and 3 and receivers 2 and 4 are on opposite sides of each other. This allows one to get two independent measurements of the w velocity component.

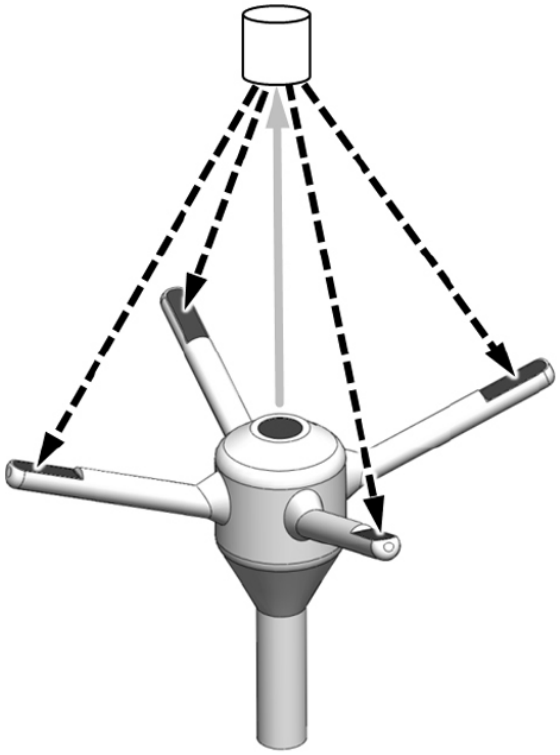

Figure 3.2: The operating principle of a four-receiver acoustic Doppler velocimeter. The transmitter in the centre of the instrument sends an ultrasound signal (the grey arrow) which is subsequently diffracted in the measuring volume (the cylinder) and recorded by the receivers. Image from Sellar et al. (2015).

In normal operation, one measurement cycle of a Nortek Vectrino consists of transmitting and receiving several individual sound pulses as well as registering the background noise level. The received signals are ensemble averaged and correlation is calculated between the individual signals. The averaging reduces random errors in the measurements. Along with the velocity, we also get two parameters for estimating the signal quality: the correlation and the signal-to-noise ratio (SNR). One measurement cycle results in one velocity value for each of the velocity components as well as correlation and SNR estimates. Low correlation usually results from a low number of scatterers in the measuring volume or a very high flow velocity. Low SNR, in turn, is usually caused by a low signal power which is also related to few scatterers. A yet another number for estimating the data quality is the signal amplitude, which is measured in signal 'counts' (Nortek AS, 2004).

The measuring probe head was placed such that the instrument head was at 0.20 metres depth with the transmitter beam facing down. The measuring volume is located 90 mm from the instrument head. The height of the volume was in these measurements about 7 mm and the diameter about 6 mm. The probe was attached to a beam, approximately 1.5 metres of length. The actual working unit of the ADV was on the raft itself. The installment of the ADV can be seen in figure 3.3.

A matter to be taken into consideration is the spatial resolution of the ADV measurement. The size of the measuring volume defines how small turbulent structures the ADV can measure as one velocity measurement is essentially an average over the volume. With a measuring volume diameter of d and mean advective velocity U, a cutoff frequency can be defined as

$$f_{\text{cutoff}} = \frac{U}{d}. \tag{3.3}$$

Any turbulent structures that occur at frequencies higher than f_{cutoff} cannot be distinguished from noise. The cutoff frequency also defines the bend in the spectrum where the actual spectrum ends and noise begins.

The instrument was set to measure at a frequency of 30 Hz. The campaign started on day 253 at 09:55 and ended on day 268 at 03:29. Data was recorded in 30-minute periods. The data

Figure 3.3: The raft in Lake Kuivajärvi with the instruments aboard. The ADV can be seen installed at the end of the beam on the left, with the measuring head in the water. The picture is taken from Erkkilä (2015).

comprises of horizontal velocity components u and v and two vertical velocity components w_1 and w_2. The z direction in the data is opposite to the direction of transmission beam, that is, the positive direction is pointed upwards. The x direction is the direction of receiver 1. y is determined by the right hand rule from x and w. In addition to the velocity, correlation and SNR values were also recorded for all components of each velocity measurement.

Although the instrument was measuring throughout the campaign, there is an unfortunate gap in the data from 02:54 on day 256 to 12:29 on day 260 due to an error in logging the data. The time series were quality checked visually for bad data, e.g. when there were people on the raft. Of the total 489 30-minute time series of ADV data, 27 were discarded for bad data quality.

A major source for errors in the data originates from so-called phase wrapping. From equation (3.2), we see that there is an ambiguity of $2\pi n$ ($n \in \mathbb{Z}$) in the measured phase difference. This means that there is a maximum measurable velocity

$$v_{\text{max}} = \pm \frac{c}{4f\Delta t} \tag{3.4}$$

where the sign $+$ refers to motion towards and $-$ away from the receiver. Velocity values outside this range will be off by $2\pi n \left|v_{\text{max}}\right|$ when they experience this phase wrapping (Lhermitte and Serafin, 1984).

3.2.2 Other instruments

Other data in this work is from permanent instruments on the raft. A thermistor chain with Vemco temperature-logging probes (Vemco, Halifax, Nova Scotia, Canada) measured water temperature at 0.2, 0.5, 1.0, 1.5, 2.0, 2.5, 3.0, 3.5, 4.0, 4.5, 5.0, 6.0, 7.0, 8.0, 10.0 and 12.0 m depth. These data are used in this work only to get an overview of the temperature profile in the lake and not for any further analysis.

Eddy correlation instruments with a sonic anemometer USA-1 (METEK GmbH, Elmshorn, Germany) and an enclosed path infrared residual gas analyser LI7200 (LI-COR Inc., Lincoln, Nebraska, USA) provided 30-minute averages of the sensible and latent heat fluxes. The sonic

anemometer data is also used for the calculation of friction velocity in the atmosphere. Radiation was measured with a CNR-1 net radiometer (Kipp & Zonen B.V., Delft, The Netherlands).

Wind speed and wind direction are measured on the raft with an anemometer and wind direction sensor. To ensure that measured flux is indeed coming from the lake and not the surrounding forests, flux records are approved when the wind direction (WD) fulfilled the condition $135 < \mathrm{WD} < 170$ or $290 < \mathrm{WD} < 345$.

A more thorough description of these instruments as well as the data preparation is provided by Erkkilä (2015).

3.3 Methods

3.3.1 Properties of water

Density of water ρ_w is a function of temperature T:

$$\rho_\mathrm{w} = \left(999.8395 + 6.7914 \cdot 10^{-2} T - 9.0894 \cdot 10^{-3} T^2 + 1.0171 \cdot 10^{-4} T^3\right) \text{ kg m}^{-3}. \quad (3.5)$$

The coefficients are from Chen and Millero (1986). The temperature in this equation is in degrees Celsius. Salinity of the water is assumed to be 0 although that is not exactly the case with lake water. Salinity wasn't measured in the campaign.

Kinematic viscosity of water ν_w is also calculated from temperature. The equation used here is

$$\nu_\mathrm{w} = 10^{-6} \left(1.7901 - 5.8729 \cdot 10^{-2} T + 1.1659 \cdot 10^{-3} T^2 - 1.0172 \cdot 10^{-5} T^3\right) \text{ m}^2 \text{ s}^{-1}. \quad (3.6)$$

The values are from fitting a third-order curve into data from Kestin et al. (1978).

3.3.2 ADV data processing methods

The ADV data processing in this work consists of the following steps:

1. Data recording.

2. Removal of phase wrapping.

3. Spike identification and interpolation.

4. Rotation to streamline coordinates.

5. Noise reduction.

6. Calculation of power spectrum, cospectrum and turbulent quantities.

Removal of phase wrapping

Phase wrapped velocities can be found and removed in the following manner. The velocity data $\mathbf{v} = \{u, v, w_1, w_2\}$ is transformed into instrument coordinates $\mathbf{v}_\mathrm{r} = \{v_{\mathrm{r}1}, v_{\mathrm{r}2}, v_{\mathrm{r}3}, v_{\mathrm{r}4}\}$. Here, $v_{\mathrm{r}i}$ is the velocity measured by each receiver i. The transformation matrix $\mathbf{T}$ in the transform $\mathbf{v}_\mathrm{r}\mathbf{T} = \mathbf{v}$ is instrument-specific and stated by the manufacturer. Any jump in the data which is larger than the preset maximum velocity difference, 0.3 m s^{-1} in this work, and which starts from values that are large enough, is marked as a start or end of phase wrapping. The corrected velocity data is then $v_{i,\mathrm{corr}} = v_{i,\mathrm{raw}} \pm 2 \cdot$ velocity range, plus or minus depending on the sign of the wrapped velocity component. The benefit of using instrument coordinates is that the amplitude of the correction is always exactly twice the velocity range. In $\{x, y, z\}$ coordinates, the magnitude of the velocity jump changes from time to time, especially if multiple velocity components experience wrapping simultaneously.

An example of the effect of phase wrapping is presented in figure 3.4. The data presented in the figure is the u velocity component. There are numerous jumps visible in the raw velocity data but the magnitude of the jumps change from one occasion to another. Also, when phase wrapping occurs over several consequtive data points, the resulting spike clearly preserved its structure. As can be seen, the de-phasewrapping method works well in restoring the data.

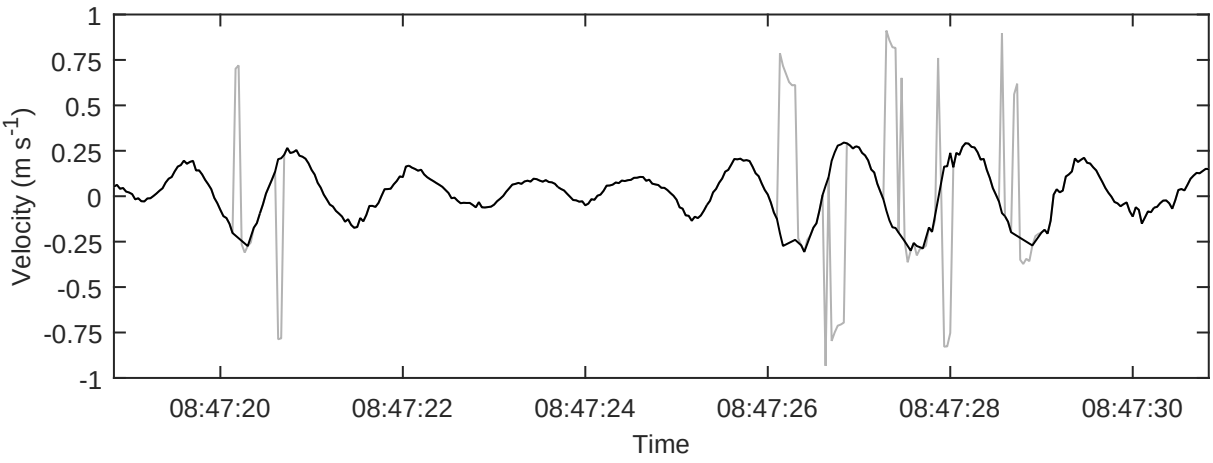

Figure 3.4: An example of the effect of phase wrapping on the u velocity component. The data is from day 265. The black line is the corrected velocity. The grey line is the raw velocity before any data handling.

Phase wrapping could be avoided in future campaigns by choosing a larger velocity range, however, this would decrease the velocity resolution. Also, it would be useful to record the data in instrument coordinates. Transforming data from $\{x, y, z\}$ to instrument coordinates and back is bound to result in rounding errors. Although these errors are likely not to be large, the best practice is still to try to minimise them by avoiding any unnecessary matrix computations.

Spike removal

Most of the spikes in the data are related to low correlation values. All data with a correlation $< 70\%$ is replaced with linearly interpolated values. According to the manufacturer, the signal-to-noise ratio should be around 10 dB and the data quality increases as SNR increases up to 15–20 dB. However, values lower than that 10 dB are not necessarily a sign of bad data (Nortek AS, 2004). Therefore, the SNR is not used as a quality criterium.

The spike identification process finds outlier data points. The data are divided into segments of 1000 consecutive data points or about 33 s. Any value of velocity component v_i that doesn't fit in the range $\langle v_{\mathrm{r}i} \rangle \pm 3\sigma_i$, where σ_i is the standard deviation, is identified as a spike. The

average and standard deviation are calculated for each 1000-point segment. This method is fast and simple and finds most spikes in the data. The identified spikes are replaced by with linearly interpolated values from adjacent data points. Spike removal is performed after the de-phasewrapping procedure so that it doesn't interfere with the procedure.

It was found that when there is a spike in one measured velocity component, all other components also contain suspicious data. However, the bad data points in some components might not fulfill the spike criterium. Thus, if one bad data value was found in any component, all data of the same index were deemed bad. In most 30-minute periods, the four velocity components had in total less than 1000 bad data points. At most, the number was 2009, which is still less than 1% of the overall data. Correlation-wise, the quality of the data can therefore be considered very good.

Coordinate rotation

The measured velocities are rotated so that the direction of u is the direction of the mean flow. In this case, the averages $\overline{v}$ and $\overline{w}$ are forced to be zero. The rotation is done to ensure that the assumptions behind equation (2.5) hold (Lorke et al., 2013).

All the velocities discussed here are $n \times 4$ matrices, n being the number of data records in one 30-minute data segment. The first rotation rotates the measured velocity $\mathbf{v_m}$ around the w component, which remains the same. The new velocity is

$$\mathbf{v_1} = \mathbf{v_m} \begin{bmatrix} \cos\theta & -\sin\theta & 0 & 0 \\ \sin\theta & \cos\theta & 0 & 0 \\ 0 & 0 & 1 & 0 \\ 0 & 0 & 0 & 1 \end{bmatrix} \tag{3.7}$$

where the rotation angle $\theta = \arctan(v_\mathrm{m}/u_\mathrm{m})$. The upper left 3×3 part of the matrix would be the rotation matrix for a three-receiver ADV.

The second rotation is around the newly calculated v_1 component:

$$\mathbf{v_2} = \mathbf{v_1} \begin{bmatrix} \cos\gamma & 0 & -\sin\gamma & -\sin\gamma \\ 0 & 1 & 0 & 0 \\ \sin\gamma & 0 & \cos\gamma & 0 \\ 0 & 0 & 0 & \cos\gamma \end{bmatrix} \tag{3.8}$$

where the rotation angle $\gamma = \arctan(w_1/u_1)$. With the Vectrino ADV, we have two independent estimates for the w component. If they both were forced to zero simultaneously, it would result in two different coordinate systems with only the x direction being common for both. Therefore, in the second rotation w_1 is used and consequently $\overline{w_1}$ becomes zero. In all further calculations except in the noise recuction algorithm, w_1 is always used as the w component.

Noise reduction

The noise reduction procedure that is applied in this work is based on the method originally presented by Hurther and Lemmin (2001) and henceforth called the HL method. The method was refined by Blanckaert and Lemmin (2006) and presented for a Vectrino ADV by Doroudian et al. (2010). The method takes advantage of the fact that since the vertical velocity w_1 is measured with receivers 1 and 3 and w_2 with receivers 2 and 4, the two measurements are statistically independent. Power spectrum of the noise can then be calculated from spectral and co-spectral densities of w_1 and w_2.

Following the notation from Hurther and Lemmin (2001), the velocity variance of the u component is

$$\overline{u'^2} = \overline{\tilde{u}'^2} + \underbrace{\frac{1}{2\sin^2(\alpha/2)}}_{a} \sigma^2, \tag{3.9}$$

where the first term on the right-hand side is the variance of the true signal and the second term is the variance of the noise. a is a geometrical factor that depends on the angle α between the

transmitted and received signals. Similarly, for variance in w component, we can write

$$\overline{w'^2} = \overline{\tilde{w}'^2} + \underbrace{\frac{1}{2\cos^2(\alpha/2)}}_{b}\sigma^2, \tag{3.10}$$

where b is the geometrical weighing factor for w. (Hurther and Lemmin, 2001)

The noise spectrum is

$$N(f) = \frac{1}{b}\left[S_{w_1w_1}(f) - S_{w_1w_2}(f)\right]. \tag{3.11}$$

and the total noise variance is

$$\sigma^2 = \int_{-\infty}^{+\infty} N(f)\mathrm{d}f = \frac{1}{b}\int_{-\infty}^{+\infty}\left[S_{w_1w_1}(f) - S_{w_1w_2}(f)\right]\mathrm{d}f. \tag{3.12}$$

The noise variance is common to all measured flow components.

The variance of a time series equals the total area of its power spectrum. We can therefore write

$$\overline{u'^2} = \int_{-\infty}^{+\infty} S_{uu}(f)\mathrm{d}f \tag{3.13}$$

and

$$\overline{\tilde{u}'^2} = \int_{-\infty}^{+\infty} \tilde{S}_{uu}(f)\mathrm{d}f. \tag{3.14}$$

Inserting equations (3.12), (3.13) and (3.14) into equation (3.9) and rearranging the terms, we arrive at

$$\int_{-\infty}^{+\infty} \tilde{S}_{uu}(f)\mathrm{d}f = \int_{-\infty}^{+\infty} S_{uu}(f)\mathrm{d}f - \underbrace{\frac{1}{\tan^2(\alpha/2)}}_{g}\int_{-\infty}^{+\infty}\left[S_{w_1w_1}(f) - S_{w_1w_2}(f)\right]\mathrm{d}f, \tag{3.15}$$

where $g = b/a$. Then, for each f, the uncontaminated spectrum is

$$\tilde{S}_{uu}(f) = S_{uu}(f) - g\left[S_{w_1w_1}(f) - S_{w_1w_2}(f)\right]. \tag{3.16}$$

In addition, the HL method can be used to correct the measured turbulent kinetic energy. The corrected TKE can be expressed as

$$\tilde{E}_k = E_k - \left(a + \frac{b}{2}\right)\sigma^2, \tag{3.17}$$

with a and b being the previously defined geometrical coefficients.

For the HL method to work, the following assumptions must hold: 1) the noise signal is white noise, i.e. its spectral density is constant over the investigated frequency range, 2) the noise is unbiased, 3) the noise is statistically independent of the velocity fluctuations, 4) the noise is uncorrelated between different velocity components, 5) $S_{w_1 w_2} < S_{w_1 w_1}$ for all f, and 6) $S_{w_1 w_1} = S_{w_2 w_2}$ for all f.

Another method for noise removal, presented by e.g. Durgesh et al. (2014), is also tested here. It is simpler than the HL method and based more on the data itself rather than the instrument. Also in this method, it is assumed that the noise has a constant amplitude at all frequencies. If the spectrum is at a constant level at the high-frequency end, the noise amplitude can be defined as the average of the spectrum at these frequencies. The amplitude of the noise can then be subtracted from the spectrum. The high-frequency end of the noise-subtracted spectrum will contain negative values, but if only the inertial subrange is used for analysis, this doesn't cause problems.

The slightly different approach to this method is that Durgesh et al. (2014) estimate the noise from the autocorrelation function. The method was also tested in this work. However, estimating the noise spectral power directly from the power spectrum proved to be a lot simpler and is therefore used here.

Chapter 4

Results and discussion

4.1 Meteorological conditions and water temperature profiles

During days 253–264 (10th–25th September, 2014), the weather was relatively warm with temperatures ranging from 14 to 18° C during days and from 3 to 7° C during nights. The wind speed varied between near-calm and 3 m s^{-1} during this period. The two prevailing wind directions were approximately 160° and 340°, that is, the wind was blowing along the lake. On day 265, a cold front passed which caused the wind direction to shift to 350° and the wind speed to increase to 3–7 m s^{-1}. The air temperatures dropped to 0–7° C. Time series of air temperature and wind speed and direction is shown in figure 4.1.

Sensible and latent heat fluxes H and LE, net longwave radiation $LW_\downarrow - LW_\uparrow$ and net shortwave radiation $SW_\downarrow - SW_\uparrow$ at the surface are shown in figure 4.2. Positive values indicate an energy flux into the lake surface, negative values a flux away from the surface. The sensible heat flux was mostly between 0 and -100 W m^{-2} (directed away from the lake surface) during days 253–264. During days 265–267, the sensible heat flux from the lake increased to values between -100 and -200 W m^{-2}. The latent heat flux behaved in a similar fashion. During days

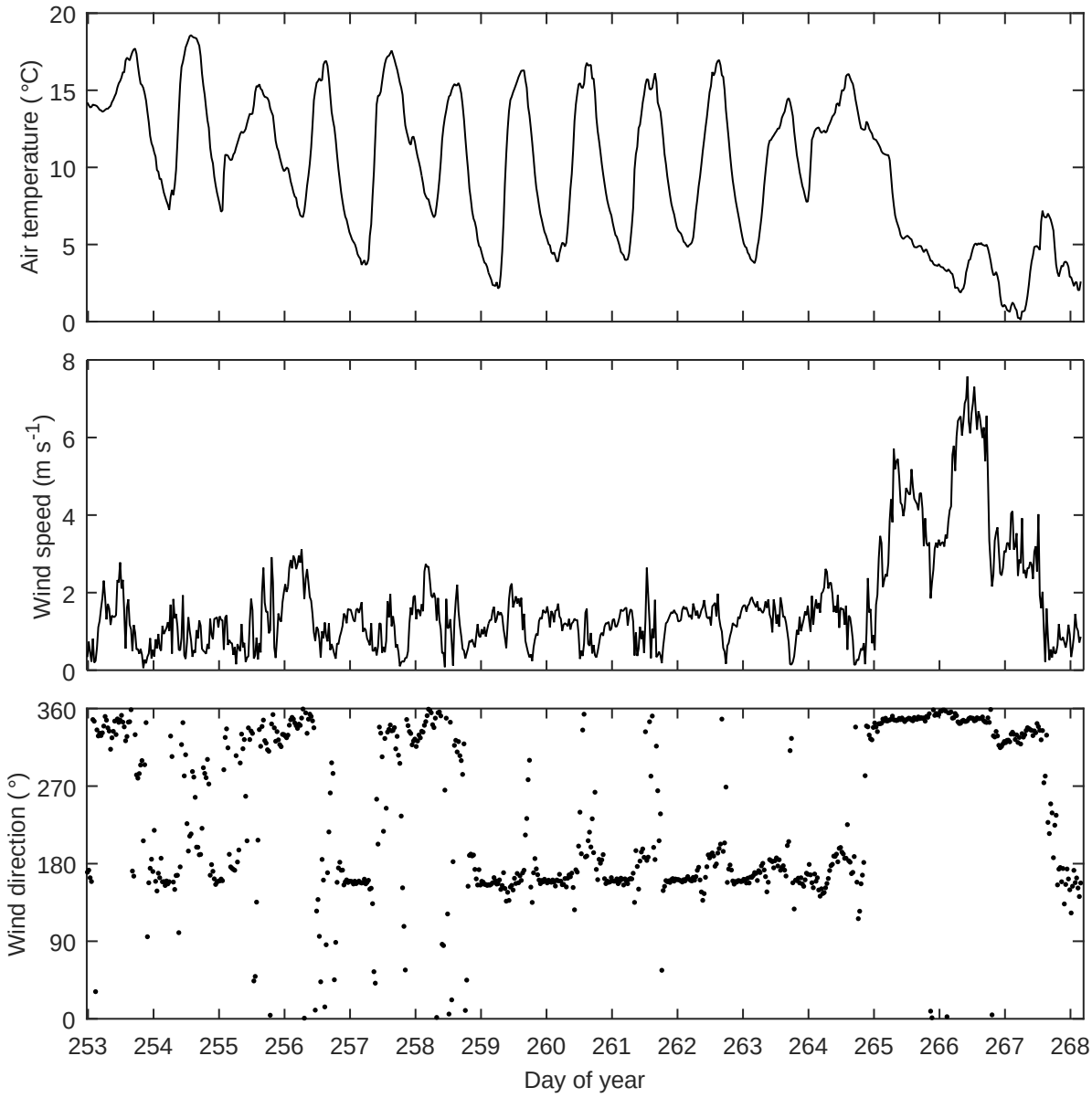

Figure 4.1: Air temperature, wind speed and wind direction during the campaign.

253–264, the flux was approximately between 0 and -60 W m^{-2} and directed away from the surface. The flux increased during days 265–267 to values of more than -200 W m^{-2}. As the flux data contains many values that don't meet the quality criteria, a large part of the final flux data is interpolated. Especially the latent heat flux during days 265 and 266 contains mostly interpolated values.

Net longwave radiation flux remained negative almost throughout the campaign, that is, away from the surface into the atmosphere. Only on day 253, the downward flux was slightly larger and the total flux was 16 W m^{-2}. The minimum longwave flux was -127 W m^{-2} on day 266. The maximum net shortwave radiation was 555 W m^{-2}. The daily maxima of the shortwave radiation varied considerably as a consequence of varying cloud cover.

The fifth panel shows the net energy flux $H + LE + LW_{\downarrow} - LW_{\uparrow} + 0.95\,(SW_{\downarrow} - SW_{\uparrow})$ into the water-side mixed layer. As pointed in section 2.1.2, $SW_{\downarrow}$ should only include the part absorbed in the mixed layer. The shortwave radiation is measured above the surface and in this work there are no measurements for how much the absorbed part accounts for the whole $SW_{\downarrow}$. According to Heiskanen et al. (2015), 95 $\%$ of incoming shortwave radiation is absorbed within the mixed layer in lake Kuivajärvi. This estimate is used also in this work.

Mean energy fluxes over the campaign period are shown in figure 4.3. All the fluxes except the the shortwave radiation are negative, i.e. the fluxes are directed from the lake surface into the atmosphere. The absolute values of the sensible heat flux have a maximum at about 5 AM and a minimum at 3 PM. The daily absolute maximum and minimum of the latent heat flux occur later than the maximum sensible heat flux, at about 1 PM and 7 PM, respectively. The mean net longwave radiation doesn't have as clear a minimum and maximum as the turbulent heat fluxes. It is at its minimum at 6 AM and at the maximum 6 PM. The mean turbulent fluxes as well as the longwave radiation are between -20 and -70 W m^{-2}. Shortwave radiation is 0 W m^{-2} during night and mean maximum at noon is about 320 W m^{-2}.

Figure 4.4 shows the water temperature profile time series. In the beginning of the campaing, until day 265, the surface was gradually cooling from almost 18°C to about 13°C. The

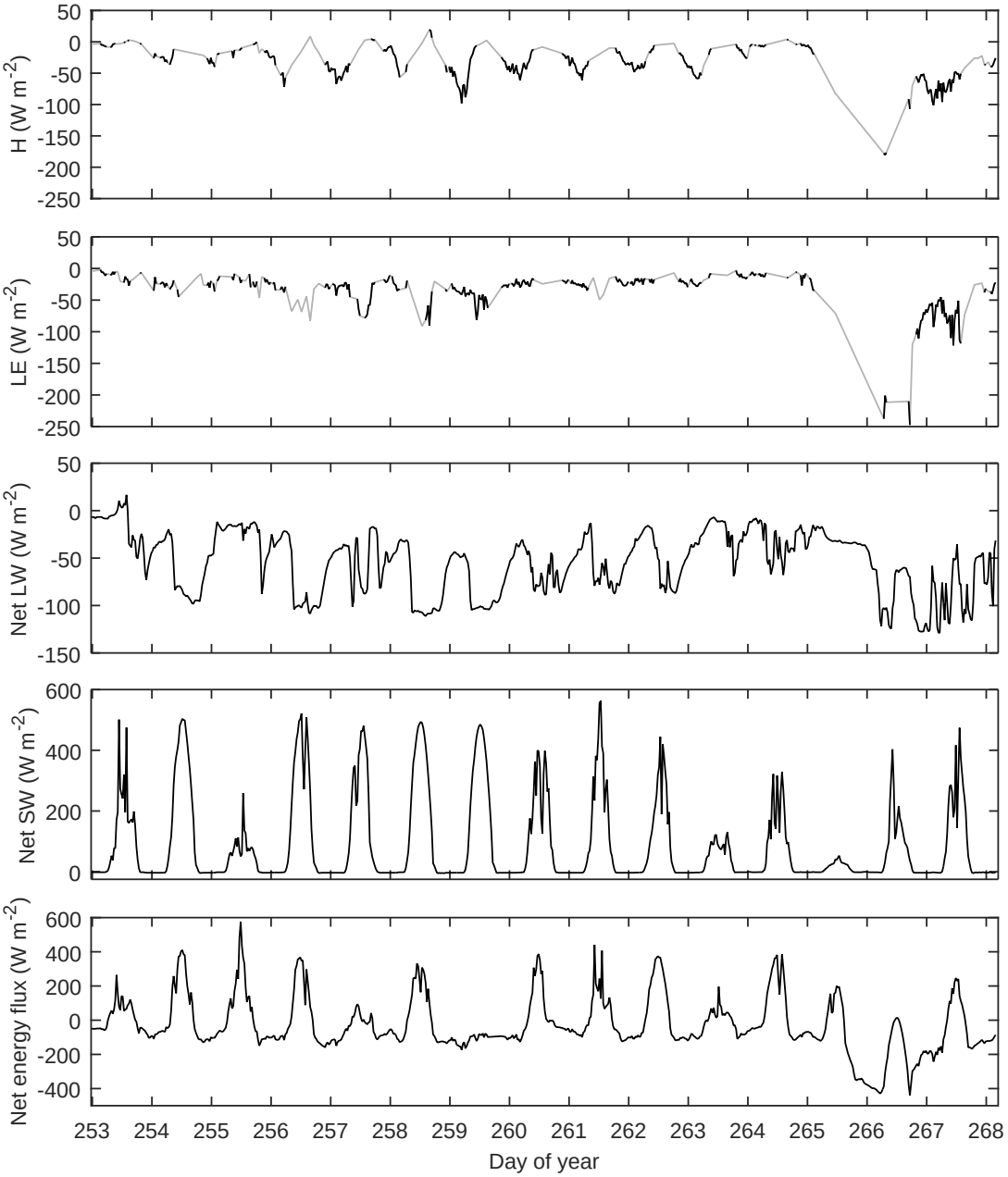

Figure 4.2: Turbulent heat fluxes, net longwave and shortwave radiation and net energy flux during the campaign. Interpolated values in the sensible and latent heat fluxes are drawn with a grey line.

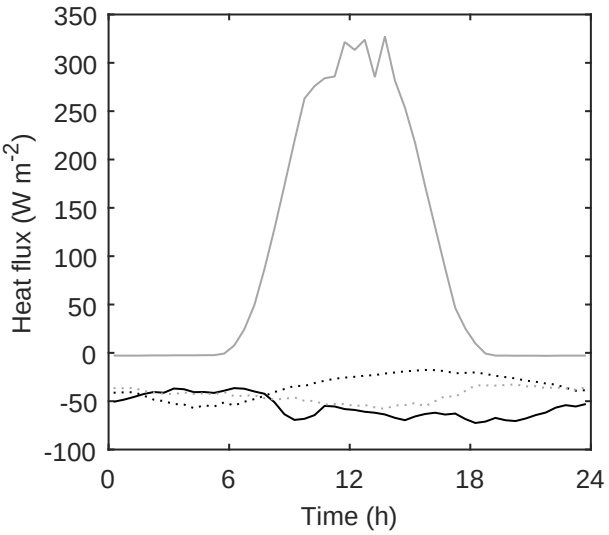

Figure 4.3: Mean turbulent and radiative heat fluxes during the campaign days. Solid black line: total longwave radiation. Solid grey line: total shortwave radiation. Dotted black line: sensible heat flux. Dotted grey line: latent heat flux. Positive values indicate a flux into the surface, negative values out from the surface.

thermocline was at a depth of about 7 m and below it, the temperature was about $8°$C. The cooling event on days 265–267 caused the thermocline to descend to about 10 m and the surface layer temperature structure to become almost homogeneous. On day 268, the temperature from the surface down to the thermocline was about $11°$C.

4.2 Velocity time series

The time series presented here are despiked, de-phasewrapped and rotated. The method for removing the phasewrapping works reasonably well and the resulting data can be used for further analysis. 21 of the 30-minute periods had so significant phasewrapping that the data couldn't be fixed.

Two examples of what the time series typically look like are drawn in figures 4.5 and 4.6. Maximum instantaneous absolute values of u and v (not shown in figures 4.5 and 4.6) are

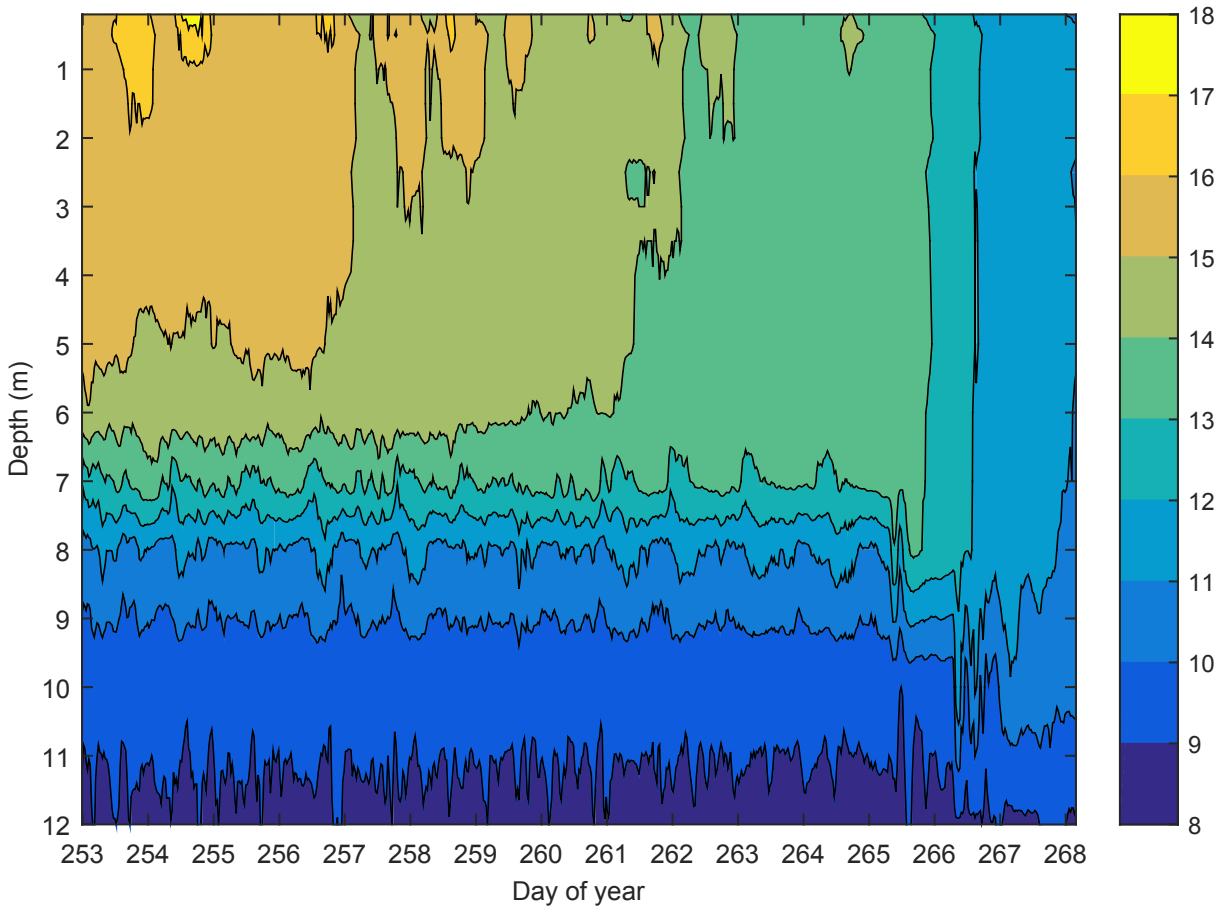

Figure 4.4: Time series of the lake temperature profile. The temperature is shown in °C.

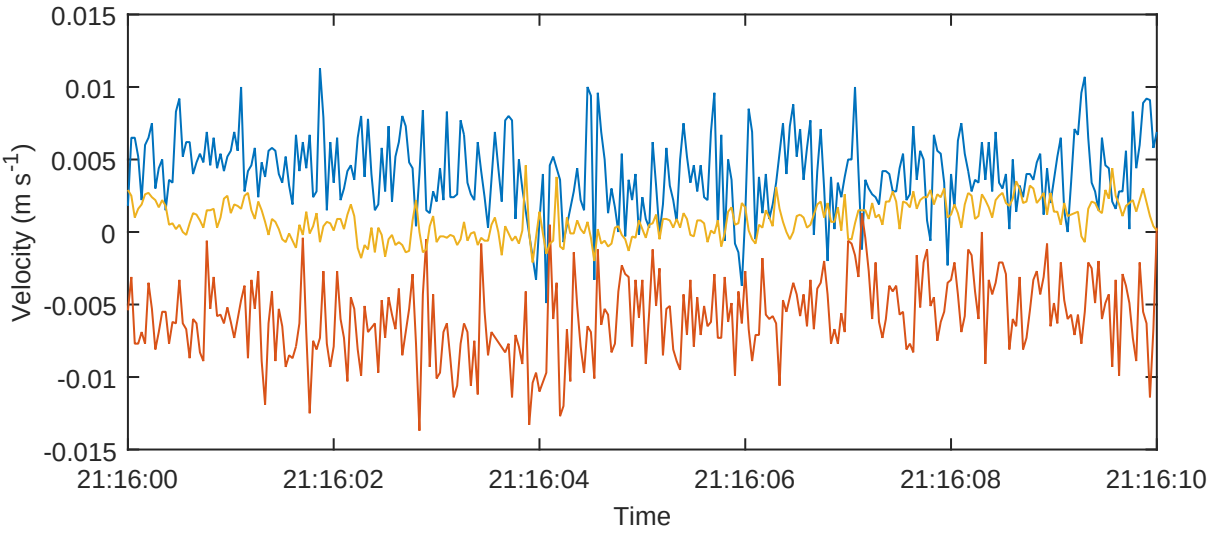

Figure 4.5: An example of the velocity time series from day 260 at 21:16. Colours for u, v and w are blue, red and orange, respectively.

0.01 m s^{-1} in calm conditions and 0.3 m s^{-1} in windy conditions. For w, the respective values are 0.2 m s^{-1} and 0.3 m s^{-1}. Differences between the vertical components w_1 and w_2 are small and one can therefore use either of them. w_1 is used as the w component in all calculations.

It is evident from figure 4.6 that there is a significant wave component present in the time series, especially during windy periods. On one hand, this is caused by surface waves in the lake. On the other hand, the wave component is caused by the raft and especially the ADV boom swaying at different amplitude than the waves. The water is therefore moving about the ADV sensor head.

Average horizontal and vertical velocities for each 30-minute period without the coordinate rotation are plotted in figure 4.7. The highest horizontal mean velocities, 0.087 m s^{-1} were measured during day 253, the first day of the campaign. The velocities were almost as high (0.069 m s^{-1}) on day 255. It is noteworthy that during the high wind period on days 265–267, the vertical velocities only increased to about 0.05 m s^{-1}. The vertical velocities stayed close to zero during days 253–264 of the campaign but became negative after the cold spell on day 265. This is the mixing event that made the temperature in the uppermost layer homogeneous,

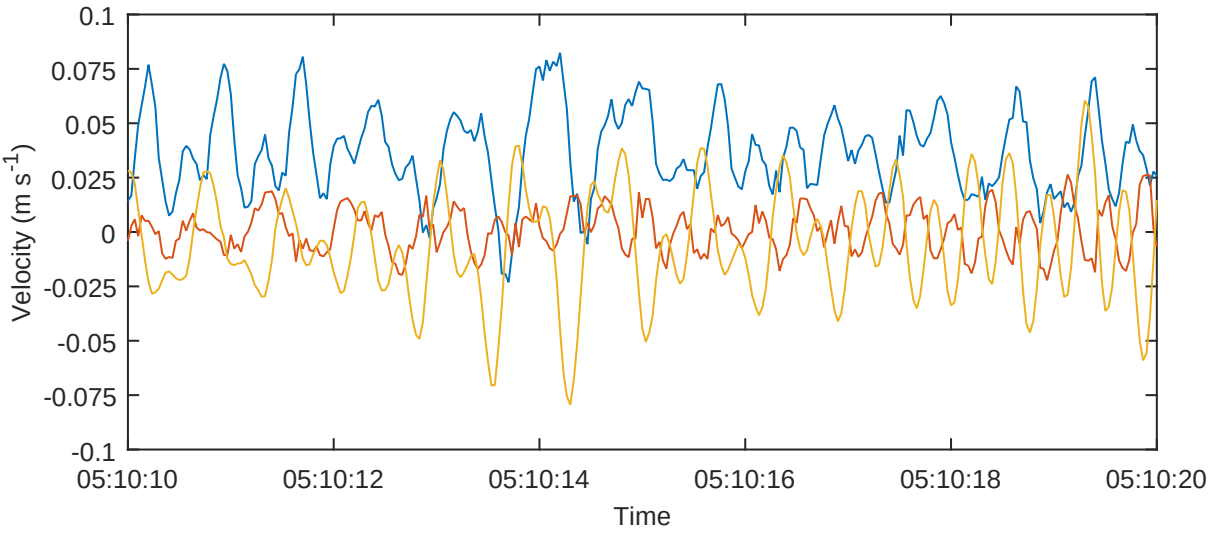

Figure 4.6: As in figure 4.5, but from day 265 at 05:10. The scale of the y axis is different from figure 4.5.

as can also be seen from figure 4.4.

The 70% correlation criterium was applied to the data. In total, only approximately 0.4% of the data was discarded. In 89% of the 30-minute segments, the mean SNR was above 10 dB and in 99% of the segments above 7 dB. These are reasonably high values and sufficient for using the data in analysis. Visual inspection of the data shows that low SNR values aren't correlated with spikes in the time series. This shows that there is no reason to use the SNR as a means of estimating data quality. However, a low SNR probably indicates that the overall power of the signal is low.

Typical numbers for signal amplitude in these data are about 20–120 counts. According to the manufacturer, the number should be above 70 (Nortek AS, 2004). This also implies that occasionally there is too little backscatter.

In clear natural waters, there is often a low number of scatterers (Blanckaert and Lemmin, 2006). This is a common problem for ADV studies. In these data, it is apparent that the low number of scatterers causes a low signal power. Common techniques for increasing the backscatter include the injection of some scattering material, e.g. sediment or microscopic air

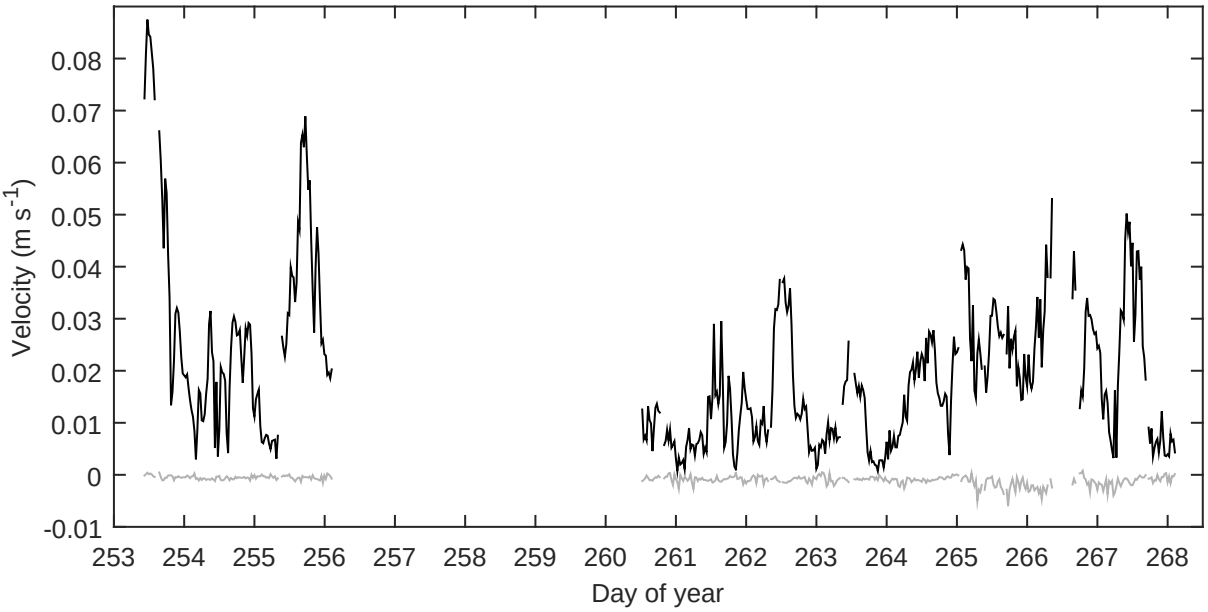

Figure 4.7: 30-minute averages of the horizontal (black) and vertical (grey) velocities. Coordinate rotation has not been used here.

bubbles, into the scattering volume (Blanckaert and Lemmin, 2006). This kind of an approach is not, however, feasible for a long-term campaign with a varying mean flow direction.

4.3 Power spectra, cospectra and turbulence parameters

4.3.1 Power spectra and cospectra

Figure 4.8 shows three examples of the power spectra S_{uu}, the HL noise-reduced S_{uu}, and S_{ww}. The spectra are averaged in 0.11 Hz frequency bins, each containing 100 points from the elementary spectra. The spectra in the first panel are from a calm period with a mean wind speed of 0.6 m s^{-1}. The noise-reduced u spectrum follows the $-5/3$ law quite well at higher frequencies. The raw spectrum is more flat at the high-frequency end. The general level of the u spectrum at frequencies > 2 Hz is about half a decade higher than that of the noise-reduced spectrum.

The spectra in the second panel are from a period where the mean wind speed was 1.5 m s^{-1}. Compared to the first panel, the S_{uu} values are higher in the low-frequency end and approximately the same at high frequencies. The raw spectrum becomes completely flat at high frequencies whereas the noise-reduced spectrum follows the Kolmogorov scaling law better.

The third panel in figure 4.8 is from a windy period, the mean wind speed being 6.4 m s^{-1}. There is a pronounced, wide peak at 0.1–2 Hz in the S_{uu} spectrum, produced by surface waves, waves reflected from the raft and the motion of the raft and the ADV itself. The values of the spectrum are higher than in the other two examples, especially at the large peak but also at both ends of the spectrum. In this spectrum, the raw spectrum at high frequencies fits well on the $-5/3$ slope. The noise-reduced spectrum has more variation.

The vertical wind component spectra S_{ww} have generally lower values than the S_{uu} spectra, meaning that the turbulence is not isotropic but the turbulent motion is more directed horizontally. Contrary to S_{uu}, the inertial subrange is more clearly seen in the w spectra, even so that in panel 3 the slope of the spectrum is greater than $-5/3$. The noise reduction is not applied to the S_{ww} spectrum because in most cases, the values of the calculated noise spectrum are larger than S_{ww}.

In most of the spectra, there is a pronounced peak at 2.67 Hz and a smaller one at 6.53 Hz. These are clearly caused by mechanical vibrations in the rigging of the ADV or elsewhere on the raft as the peak frequencies remain the same from one spectrum to another. They weren't filtered out in this analysis as it was outside the purpose of this work. In calculating the viscous dissipation, the frequency range was chosen so that these peaks were avoided.

The velocity cospectra also have similar peaks as the power spectra at the wave frequencies, approximately $0.1 \ldots 1\text{s}^{-1}$, and at 2.67s^{-1} as can be seen in figure 4.9. As the area of the cospectrum S_{uw} equals the covariance $\overline{u'w'}$, the wave peaks increase the covariance estimates. Waves and raft movement therefore have a significant impact on the measured momentum flux τ (equation (2.8)).

Most of the values of the cospectrum in figure 4.9 are positive and the total area of the

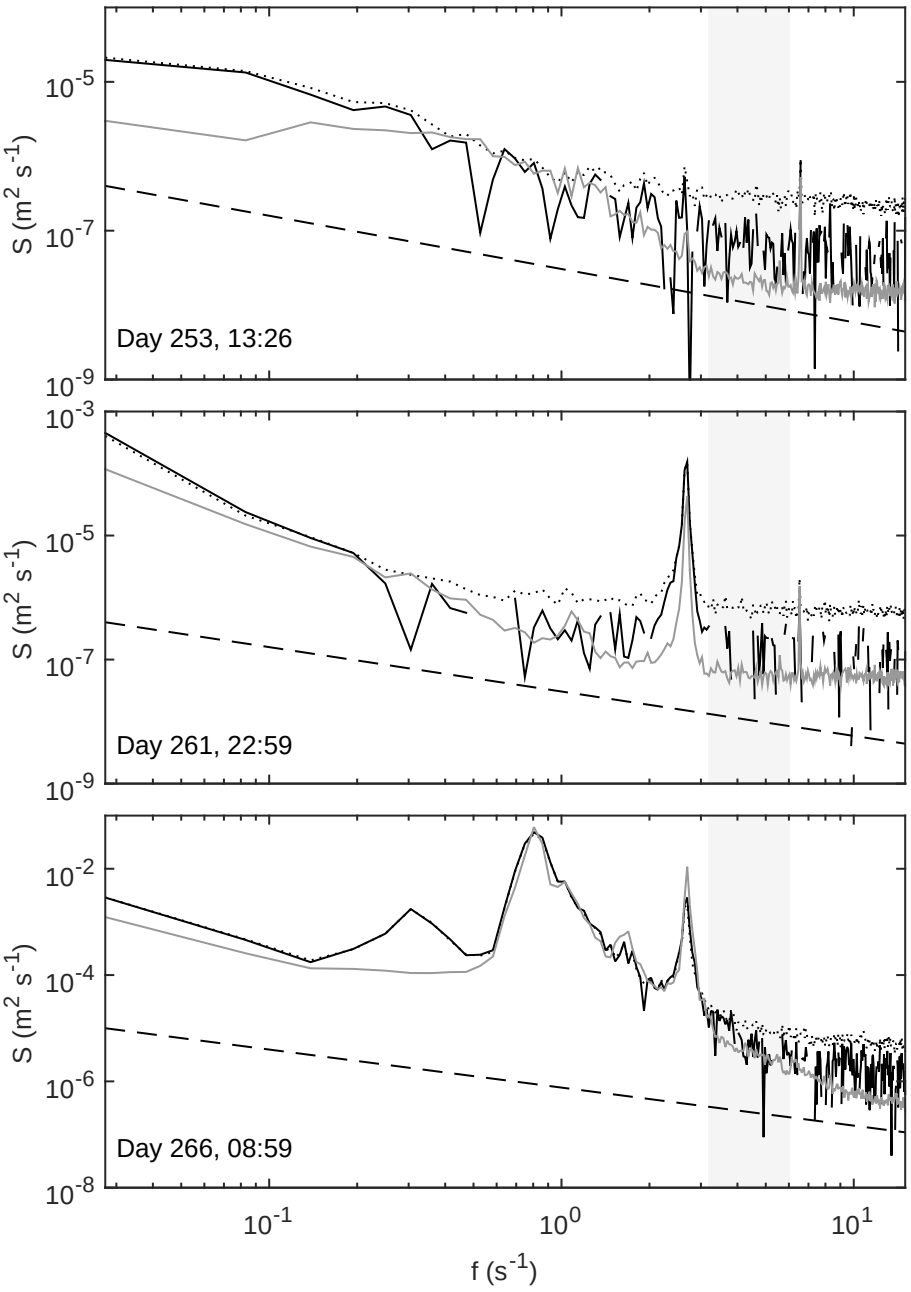

Figure 4.8: Three examples of power spectra. S_{uu} without noise removal (dotted line), S_{uu} with HL noise removal (solid black line) and S_{ww} without noise removal (solid grey line). The dashed black line shows the $-5/3$ exponential curve. The light-grey area is the frequency range used in the calculation of dissipation rate. Note that the vertical scales are different.

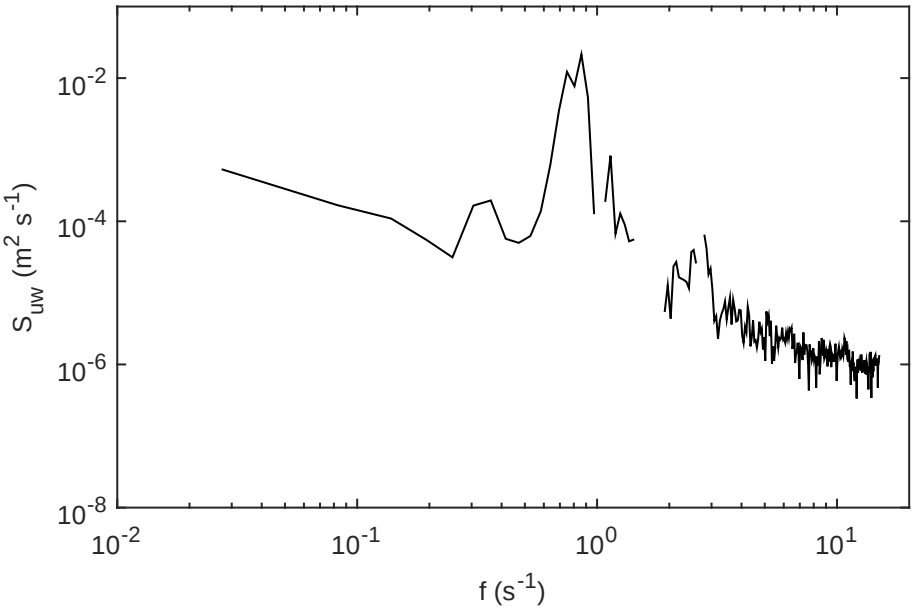

Figure 4.9: Cospectrum of u and w from day 266 at 04:59. The mean wind speed was 5.5 m s^{-1}

cospectrum is also positive. This is true for most of the other cospectra as well. It indicates that the Reynolds shear stress in equation (2.6) is negative. This, in turn, means that there is an upward net transfer of momentum in the lake and therefore a horizontal velocity profile that increases downward at least close to the surface. One possible explanation for the flow in the lake is that the lake is almost a closed system. When wind pushes the surface water to one side of the lake, the water at a greater depth must flow in the opposite direction.

The wave and vibration peaks weren't filtered out in the analysis. Removing especially the wave peaks can be difficult. As can be seen from panel 3 figure 4.8, the peaks strech over one decade of frequency. It is first of all difficult to estimate the frequency range where the waves exist and, secondly, impossible to estimate how much power each wave component has.

Despite of the noise removal, we see from the power spectra that there is often too much noise with respect to the signal. Especially in calm conditions, the flat noise part of the spectrum extends to frequencies of a few Hz. The same can be shown by calculating the cutoff frequency with equation (3.3). An example of this is the top panel of figure 4.8. In this case, the signal

power is also close to the noise power. Consequently, the measurement amplitude and the SNR are low.

4.3.2 Friction velocity

A time series of the friction velocity in water, $u_{*,\mathrm{w}}$, along with the scaled friction velocity in air, $\sqrt{\rho_\mathrm{a}/\rho_\mathrm{w}}u_{*,\mathrm{a}}$, is shown in figure 4.10. There are clearly two different regimes: the high-wind regime on days 265–267 when the friction velocity in water was generally larger than the scaled friction velocity in air, and the low-wind regime on days 253–264 when the situation was the opposite except for a few cases.

The friction velocities are compared to each other in figure 4.11 according to equation (2.18). Only a few u_* pairs lie on the 1:1 line. The two wind regimes are clearly visible as the two groups of dots, one above the line and the other below it. However, despite the differences, $u_{*,\mathrm{w}}$ and the scaled $u_{*,\mathrm{a}}$ are within the same decade. The values of $u_{*,\mathrm{w}}$ vary between $3 \cdot 10^{-4}$ and $5 \cdot 10^{-2}$ m s^{-1}.

In a high-wind regime, waves affect the measured velocity covariances and increase the co-spectral area. Consequently, also the friction velocity estimates u_* are thus increased. Because the wind is measured at a height of 2 m above the water, the effect of waves on $u_{*,\mathrm{a}}$ is likely much smaller on the wind measurements. The fact that $u_{*,\mathrm{w}} > \sqrt{\rho_\mathrm{a}/\rho_\mathrm{w}}u_{*,\mathrm{a}}$ during strong wind can be explained by the effect of waves, the term τ_wave in equation (2.37).

Normally in water, turbulence is strongest at the surface and decays exponentially when the depth increases. The ADV measured the water velocity at 29 cm away from the surface. When waves are not present or their effect is small, the measured turbulence will be smaller than directly at the surface. In low-wind or calm conditions, we can therefore expect to see a smaller $u_{*,\mathrm{w}}$ than $\sqrt{\rho_\mathrm{a}/\rho_\mathrm{w}}u_{*,\mathrm{a}}$.

Calculating the $u_{*,\mathrm{w}}$ from $u_{*,\mathrm{a}}$ is, when lacking direct measurements in water, a common practice. At the depth of the ADV, the scaling equation (2.18) holds depending on the conditions. The possibility of an imbalance of the friction velocities should be taken into account.

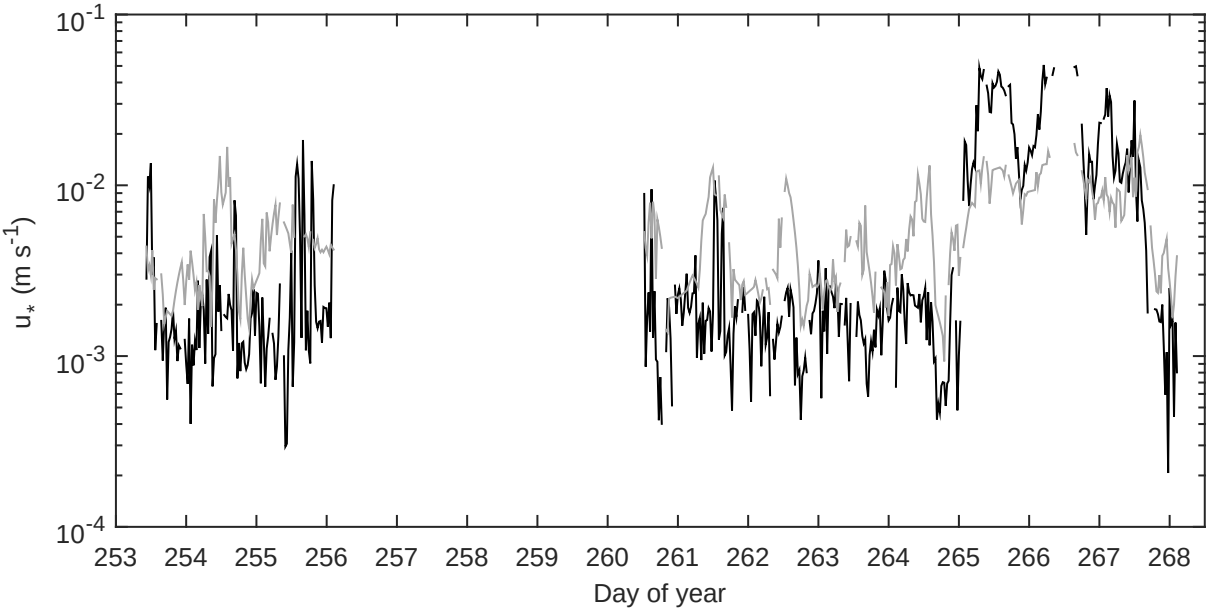

Figure 4.10: Water friction velocity measured by ADV (black) and the estimated air-side friction velocity according to equation (2.18) (grey).

4.3.3 Viscous dissipation

The frequency range used in calculating the dissipation rate with equation (2.34) is 3.2–6.0 Hz. The range was chosen visually from the spectra (figures 4.8 and 4.9) so that it's on the high-frequency side of the wave peaks and also that it doesn't have any permanent peaks caused by vibration. A constant frequency range is chosen for simplicity. In similar studies, such as Vachon et al. (2010) and Bluteau et al. (2011), the inertial subrange was found in approximately the same frequencies.

The viscous dissipation is calculated with equation (2.34) from the spectrum within the chosen inertial subrange and then calculating the mean. This method is not completely correct because it is then assumed that the spectral estimates $S(f)$ are normally distributed when, in fact, they obey the χ^2 distribution (Bluteau et al., 2011). Taking the mean as an estimate for ε is chosen for its simplicity. Also, the error induced is likely small.

Figure 4.12 shows the determined dissipation rates ε_u (from S_{uu}), ε_w (from S_{ww}) determined

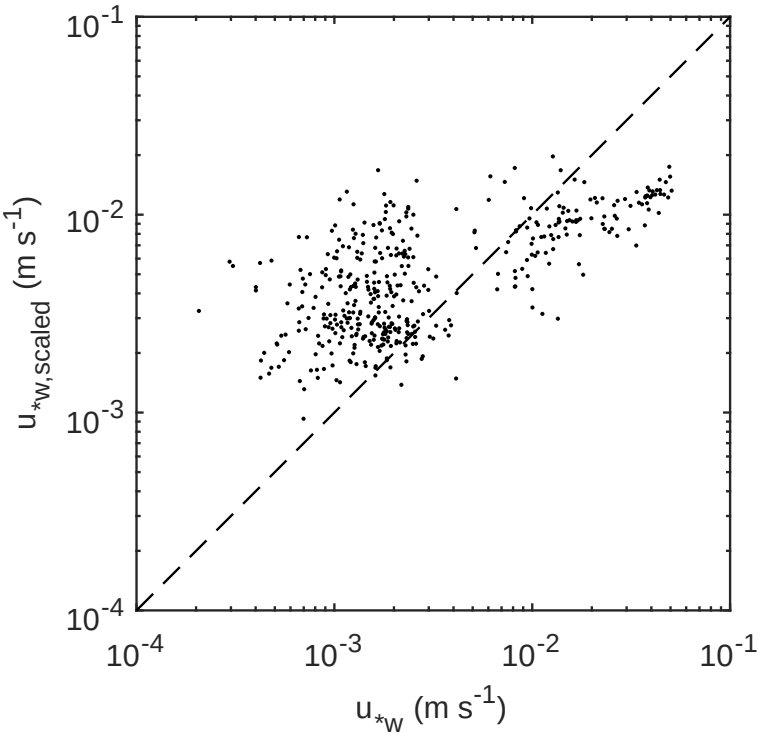

Figure 4.11: Comparison of the water friction velocity measured by ADV and the estimated air-side friction velocity according to equation (2.18).

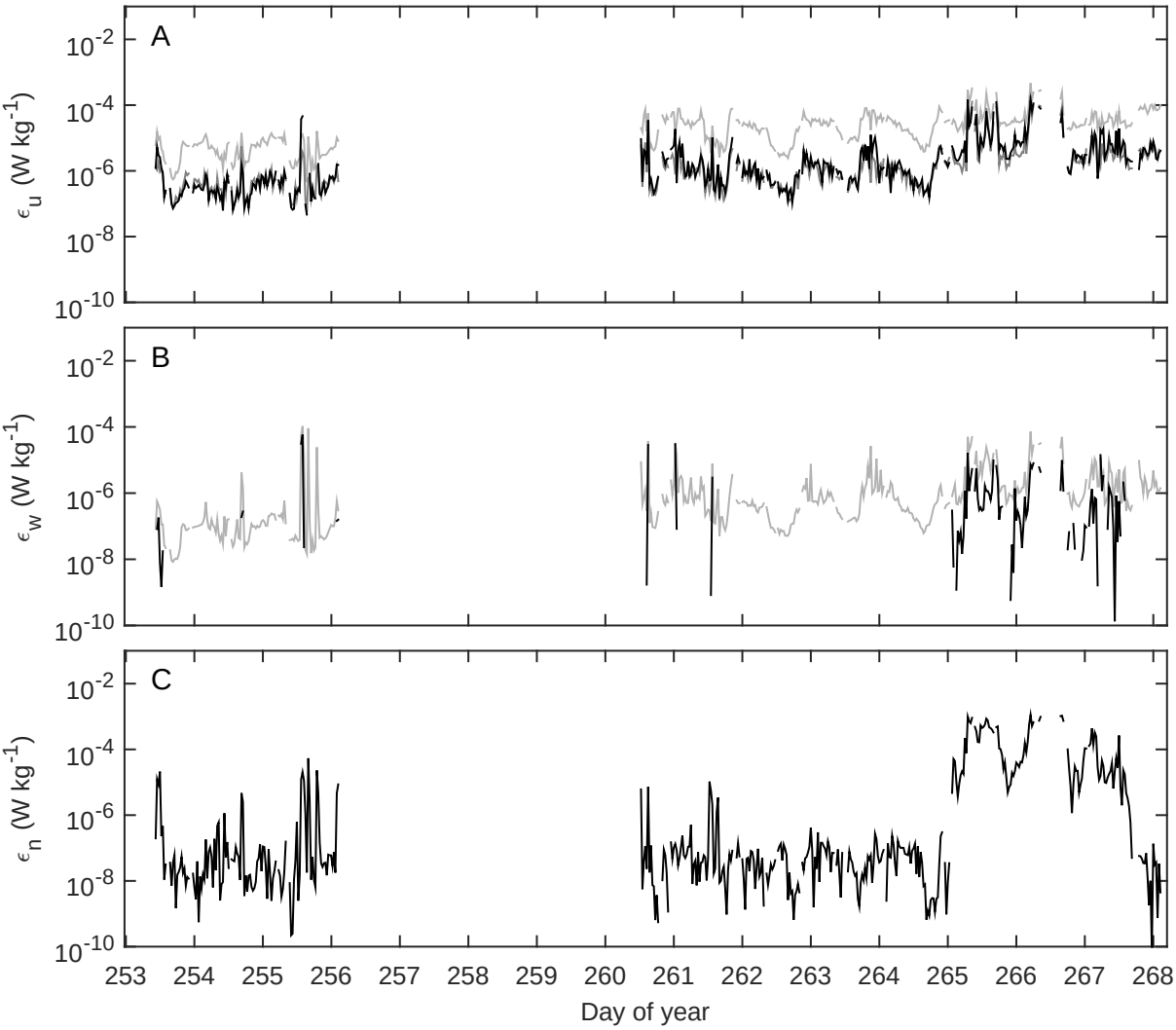

Figure 4.12: Dissipation rates. A: ε from the raw S_{uu} spectrum in light grey, from HL noise-reduced spectrum in black and from constant noise reduction in dark grey (almost under the black line). B: ε from raw S_{ww} spectrum in light grey and with the HL noise-reduction in black. C: neutral ε.

from the inertial subrange with equation (2.34) and also the neutral dissipation rate ε_{n} from equation (2.21). With the ε_u, the two noise-reducing methods are used and with the ε_w, only the HL (Hurther and Lemmin, 2001). No noise-removing method is applied to the ε_{n}. All dissipation rates except the ε_{n} have additionally been divided by the correction terms (2.35) and (2.36).

The values of ε_u are between the order of 10^{-7} and 10^{-3} W kg^{-1} with the highest values towards the end of the campaign. ε_w is most often smaller than ε_u. The difference between ε_u and ε_w is about one decade. ε_{n} during days 253–264 is generally smaller, of the order of 10^{-7} W kg^{-1}, than ε_u. It increases to values of up to 10^{-4} W kg^{-1} on days 265–267.

Dissipation rates in have been measured with acoustic Doppler velocimetry by numerous authors. Vachon et al. (2010) determined ε to be of the order of $10^{-6} \ldots 10^{-5}$ W kg^{-1} in an alpine lake. MacIntyre et al. (2018) reported smaller dissipation rates, $\sim 10^{-9} \ldots 10^{-7}$ W kg^{-1}, in an arctic pond. Examples of measuring ε at sea include Bluteau et al. (2011) with $\varepsilon \sim 10^{-8} \ldots 10^{-5}$ W kg^{-1} and Durgesh et al. (2014) with $\varepsilon \sim 10^{-6} \ldots 10^{-4}$ W kg^{-1}. Studies in lakes with microstructure profiles, such as Kocsis et al. (1999) and Sander et al. (2000), reported the dissipation rates closest to the surface to be $\sim 10^{-7} \ldots 10^{-6}$ W kg^{-1}.

Sunderland and Melville (2015) also measured dissipation with an ADV. Dissipation rates were as high as $\sim 10^{-3} \ldots 10^{-2}$ W kg^{-1} but they were measured in the open ocean with breaking waves and with significant wave heights ranging from one metre to several metres. We can conclude that the highest dissipation rates, $\sim 10^{-3}$ W kg^{-1}, in this work are definitely too high. It also seems unlikely that $\varepsilon \sim 10^{-4}$ W kg^{-1} could be realistic in a lake.

Having constant boundaries for the inertial subrange in all the different conditions is not the optimal solution. The location of the subrange is also a matter of discussion. Some authors, such as Bluteau et al. (2011), apply methods which determine the inertial subrange boundaries individually for each case. MacIntyre et al. (2018) also use a moving inertial subrange and utilise spectral fitting in determining the dissipation rate. In both of these studies, the inertial subrange can be at frequencies that are 1–2 decades smaller than in this study. Avoiding the

noise part of the spectrum would result in smaller and probably more realistic dissipation rate estimates. On the other hand, the effect of waves in the chosen inertial subrange could then be significant.

4.3.4 Noise removal

The estimated dissipation rates are used to compare the different noise-removal methods. The different ε values are shown against each other in the scatter plots in figure 4.13. When ε estimates are calculated from the spectrum, applying the HL noise removal method and also including the correction function results in decreasing the estimates by about one or even two decades, as is shown in panel A. The two methods for removing noise, HL method and constant noise substraction, give almost similar results for ε. This is shown in panel B.

As was mentioned earlier, turbulence doesn't seem to be quite isotropic but more directed in the horizontal direction. In panel C in figure 4.13, most of the εs from HL noise removed S_{uu} spectrum are larger compared to the dissipation rates from the S_{ww} without any noise-removal. This is further evidence of the more horizontally directed turbulence.

The neutral dissipation rate and dissipation rates from the other methods aren't very much related. Panel D shows that most of the ε pairs lie far away from the 1:1 line. However, this could be an expected result because we don't know anything about the stability.

Coefficients of determination (R^2) and the respective p values for a least-squares fit between the ε pairs are shown in table 4.1. With an acceptable p value of $p \leq 0.05$, all of the fits except HL noise-reduced S_{uu} and the neutral ε are statistically significant. In panel C, the fit between dissipation rates determined from the u and w spectra is not especially good.

A noteworthy matter in the noise-reduced spectra is that they often have unphysical negative values at the high-frequency end. This can be seen also in all of the panels in figure 4.8 as gaps in the spectra. The negative values outside of the high-frequency part of the spectrum imply that the HL noise-reducing method doesn't always work but instead overestimates the values of the noise spectrum. Also the constant noise method will result in negative values in the noise part

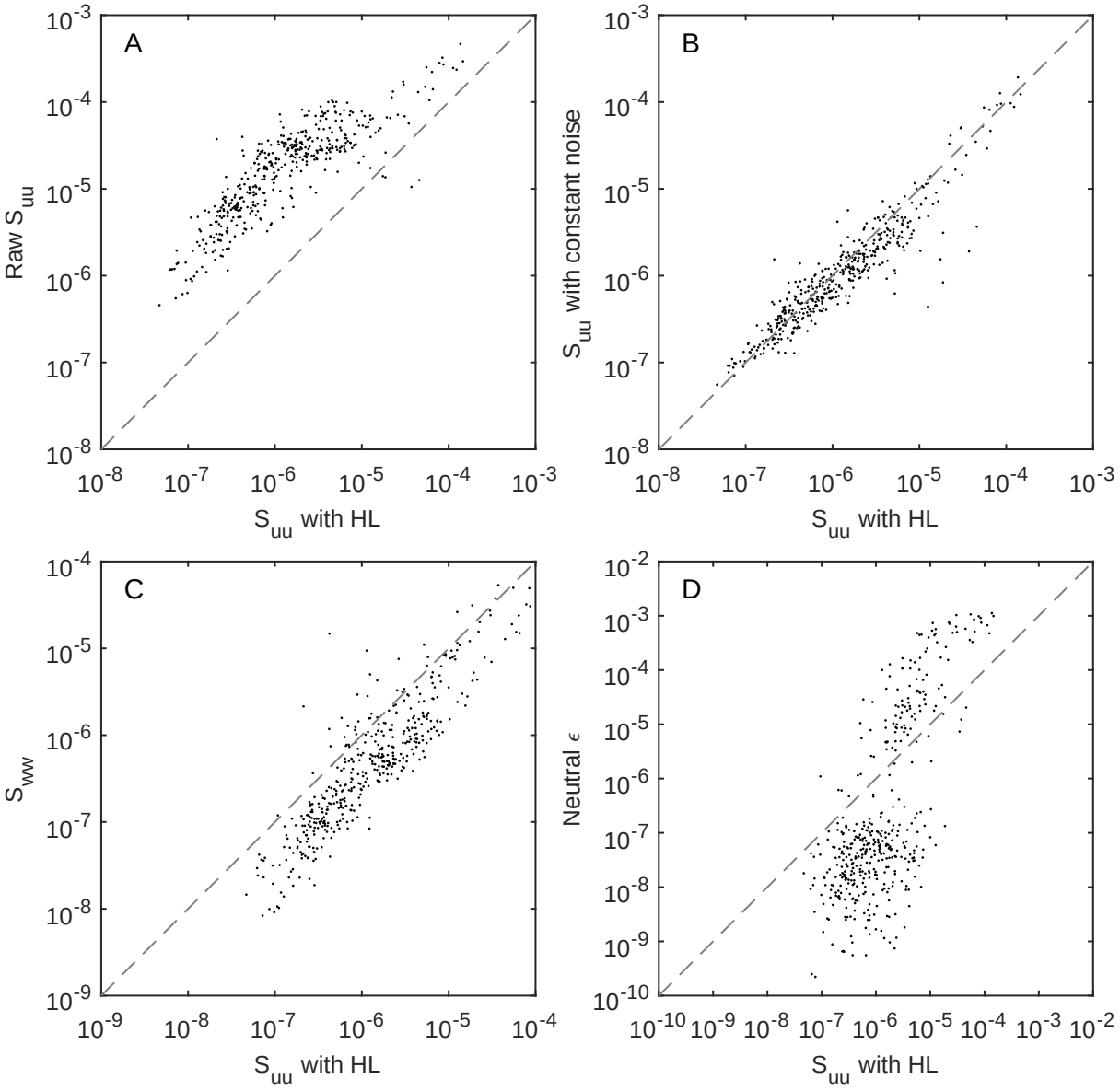

Figure 4.13: Comparison of dissipation rates from the HL noise-substracted spectra and other methods. The dashed lines mark the 1:1 relation.

Table 4.1: Coefficients of determination (R^2) and p values between different dissipation rates. 'Panel' refers to figure 4.13.

Panel	R^2	p
A	0.74	≈ 0
B	0.87	0.04
C	0.46	0.02
D	0.61	0.23

of the spectrum. On the other hand, the noise part of the spectrum doesn't contain information about the turbulent quantities. Therefore, the negative values aren't necessarily a problem.

As most of the determined dissipation rates are very different, it isn't really possible to assess which ones are the correct ones. The method that is presented in this work requires therefore improvement. For example the choise of the inertial subrange is a matter of question.

The fact that the noise spectrum N has values that are larger than S_{ww} is a sign that the HL noise-removal doesn't work perfectly. More work should be done in assessing whether the underlying assumptions actually hold. For example, because the turbulence is more directed horizontally, the noise component might also be larger for S_{uu} and S_{vv} than for S_{ww}.

Although one of the assumptions behind the HL method is that the noise is constant for all velocity components, this is clearly not the case here, as the noise spectrum is almost always larger than S_{ww}. This can be seen in panel B, where only a few values of ε are positive. The constant noise subtraction for S_{ww} could have given better results, however, it was not applied. In panel C, the neutral dissipation rate has similar high and low-wind regimes as the friction velocity.

Figures 4.8 and also 4.12 show that removing noise from the spectra is essential before calculating the dissipation rate from the spectrum. Without this, the noise will be a major error source. Of course, one should be careful in choosing the right method: for example, the HL method might overestimate the noise as the S_{ww} spectrum shows. The use of the neutral

dissipation rate requires information on the stability. In low-wind conditions, the flat noise part of the spectrum extends all the way to the selected inertial subrange. Because the constant slope of 0 is larger than $-5/3$, this results in the overestimation of the dissipation rate when using equation (2.34). Choosing improper frequencies for the inertial subrange is also a source for errors.

4.3.5 Turbulent kinetic energy

The turbulent kinetic energy (TKE) is shown in figure 4.14. The raw TKE as well as the noise-reduced TKE are both drawn. TKE varied in the range $10^{-7} \ldots 10^{-3}$ J kg^{-1} during days 253–265 and in $10^{-3} \ldots 10^{-2}$ J kg^{-1} on days 265–267.

Apart from a few cases, differences between the raw TKE and noise-reduced TKE are not large. It is obvious from the figure that the HL noise reduction fails during the high-wind period of days 265–267 because the values of the noise-reduced TKE are higher than in the raw spectrum.

Time series of the shear production and buoyancy fluxes are presented in figure 4.15. The shear production P_S is estimated using equation (2.21) with $z = 0.29$ m, $k = 0.40$, and u_* obtained from equation (2.15). This is not quite correct, as equation (2.21) only applies to situations where the stratification is neutral. It is, however, used here as an approximation since no better estimate is available. The buoyancy flux, J_B, is obtained from above-surface flux measurements using equation (2.13). During days 253–264 and 267, the buoyancy flux was about $1 \ldots 2 \cdot 10^{-7}$ W kg^{-1} and became slightly negative during nighttime. Buoyancy flux was negative, about $-1 \cdot 10^{-7}$ W kg^{-1} on days 265–266. The shear production was of the order of 10^{-8} and 10^{-7} W kg^{-1} on days 253–264 but increased to even 10^{-3} W kg^{-1} during the high-wind period of days 265–267.

The simplified TKE equation $P_\mathrm{S} + J_\mathrm{B} = \varepsilon$ is in most cases not in balance, as can be seen from figure 4.16. Shown here is the ε_u determined with equation (2.34), noise-reduced using the HL method and further divided with the correction function $F_u(I)$ of equation (2.35). Reasons

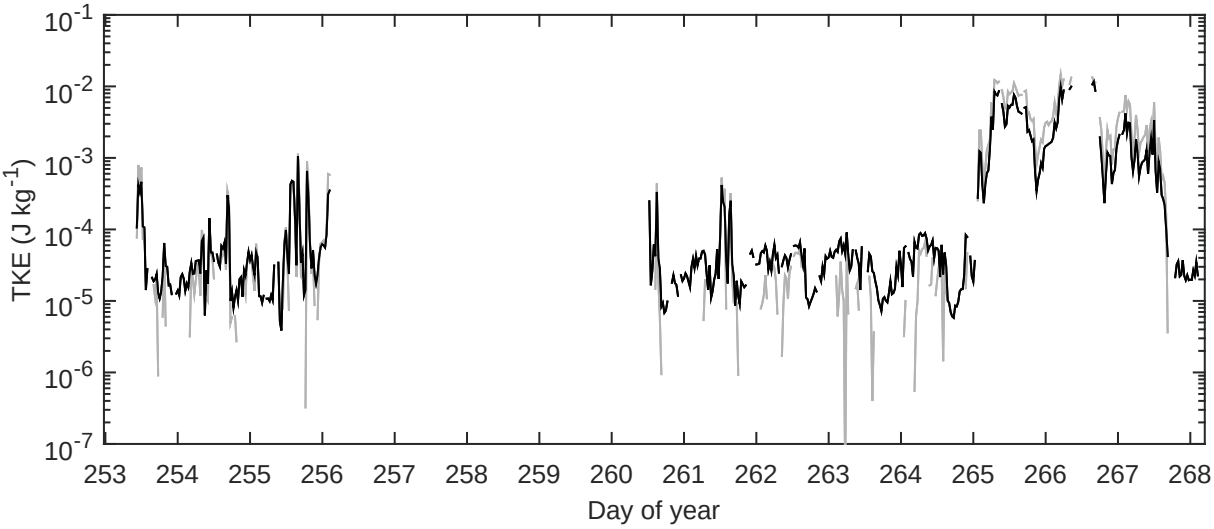

Figure 4.14: Turbulent kinetic energy. Raw TKE in black, HL noise-reduced TKE in grey.

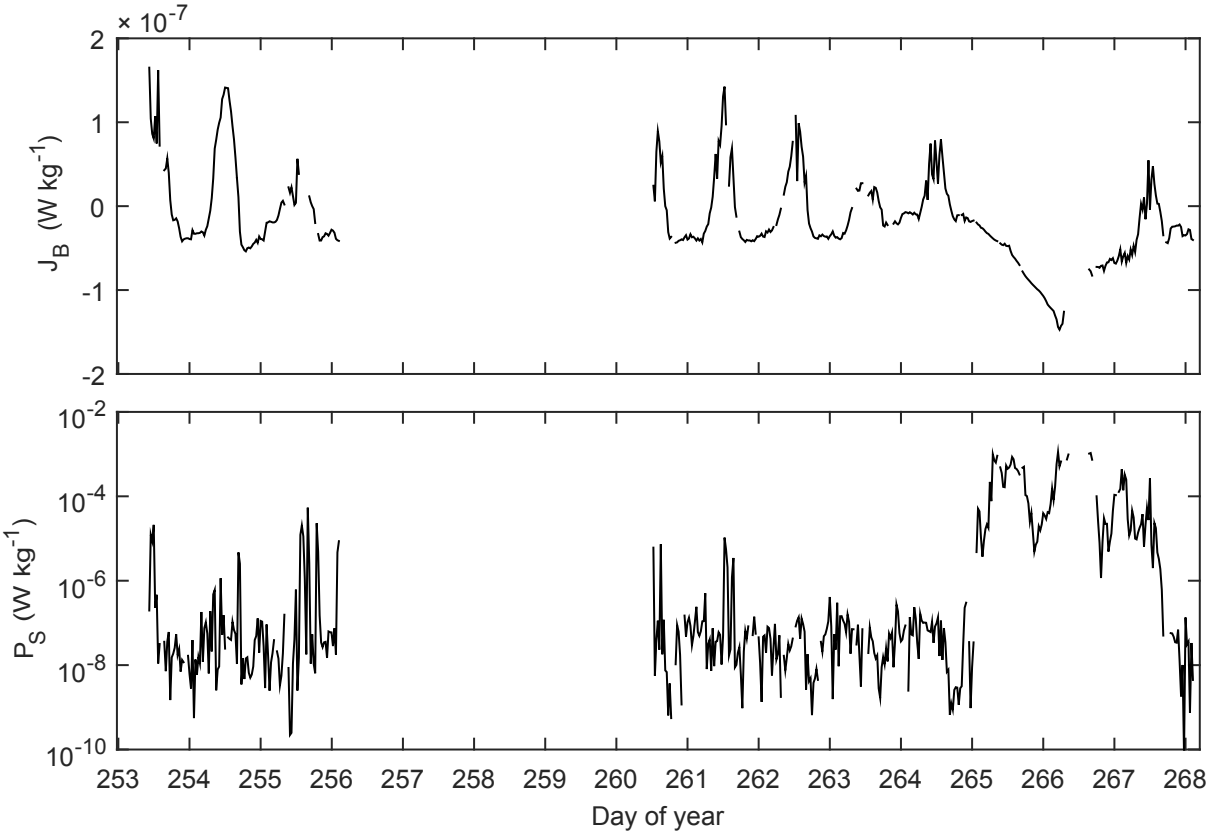

Figure 4.15: Buoyancy flux J_{B} and shear production P_{S}. Note that the scales are different.

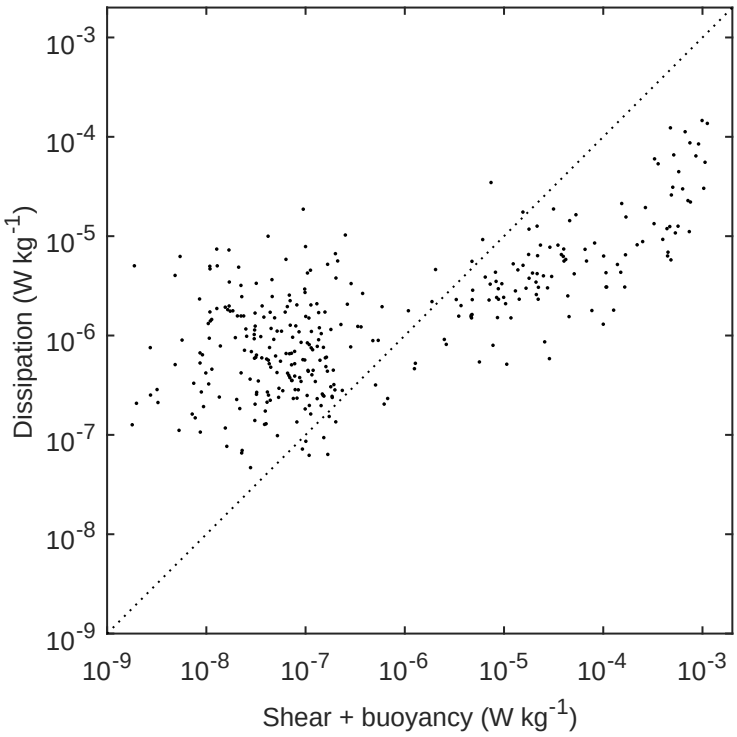

Figure 4.16: $P_{\mathrm{S}} + J_{\mathrm{B}}$ against the HL-corrected ε_u. The 1:1 relation is marked with the dotted line.

for the imbalance are most importantly related to the wind speed. The high-wind cases are located on the right and centre in the figure. Calm and moderate cases are on the left. During high winds, the shear is very large due to the effect of surface waves on the friction velocity. During low winds, the dissipation rates might be overestimated, perhaps an effect of noise in the spectrum.

Another question is whether the exclusion of the transport terms in the TKE equation (2.12) can be justified. If the lake is not homogeneous enough in the flow direction, the transport terms are of importance. Durgesh et al. (2014) compared turbulence production with the dissipation but didn't exclude the transport terms or the total derivative of TKE from the equation. For some further analysis, for example similarity scaling of turbulence in the surface layer, the simplified form of the TKE equation (2.20) is, however, required.

Chapter 5

Conclusions

High-frequency velocity measurements with an acoustic Doppler velocimeter (ADV) were carried out in Lake Kuivajärvi in southwestern Finland in September 2014. The campaign lasted 16 days, from the 10th to the 25th of September. In total, the campaign resulted in about ten days of ADV data. The meteorological forcing had two distinct regimes during the campaign: a relatively calm and warm period during the first 13 days and a cold and windy period during the last three days. The windy period caused substantial cooling in the lake and made the temperature profile homogeneous.

During the low-wind period, the friction velocity was estimated to be $3 \cdot 10^{-4} \ldots 2 \cdot 10^{-2}$ m s^{-1}. The scaled friction velocity in air was mostly larger than in water. During the high-wind regime, the friction velocity was $2 \cdot 10^{-3} \ldots 5 \cdot 10^{-2}$ m s^{-1}. The friction velocity in water was larger than the scaled friction velocity in air. The differences were likely caused by waves during the high-wind period and suppressed turbulence in water during the low-wind period. The assumption that u_* in water can be calculated from u_* in air might not hold in all conditions, even close to the surface.

The viscous dissipation rate was determined from inertial subrange in the u and w velocity component spectra, as well as using the neutral estimate for the dissipation. Noise-removal methods and correction functions were applied to the estimates. Dissipation rate was estimated

to be $\sim 10^{-8} \ldots 10^{-4}$ W kg^{-1} with different inertial subrange methods in the low-wind regime. The neutral dissipation rate was estimated to be $\sim 10^{-10} \ldots 10^{-5}$ W kg^{-1}. During the high-wind period, the dissipation rate estimates were $\sim 10^{-7} \ldots 10^{-4}$ W kg^{-1} using the inertial subrange methods and $\sim 10^{-6} \ldots 10^{-3}$ W kg^{-1} using the neutral dissipation rate. It is likely that at least the highest dissipation rates ($\sim 10^{-4}$ W kg^{-1}) are overestimated. The overestimation was probably caused by the effect of waves in the inertial subrange and also measurement noise.

A simplified turbulent kinetic energy equation with dissipation rate, shear production and buoyancy production was tested as well. The equation was generally not in balance. In the low-wind regime, dissipation rate was generally higher than the turbulence production. The situation was opposite during the high-wind period. The overestimation of the dissipation rates may have caused the imbalance during the low-wind period. During high winds, the shear production may have been estimated too high. Also, the equation should perhaps include turbulent transport terms as well.

It is shown in the work that utilising noise-removal methods is essential in ADV measurements. Two different methods were tested. It could not be demonstrated which method should be used.

In future studies, the noise-removal methods could be further refined as there was still noise left in the data. Mechanical vibrations in the rigging of the ADV should be removed of at least minimised. A better installment would have the ADV looking up and perhaps following the surface of the water. The dissipation rate estimates should be refined. A better method would include varying boundaries for the inertial subrange. Also, different spectral fitting methods could be used.

As such, this work gives insight into acoustic Doppler velocimetry and questions related to it. It was stated by Sunderland and Melville (2015) that measuring turbulence close to the water surface is 'notoriously difficult'. That statement was proven to be true in this study.

Bibliography

Bendat, J. S. and A. G. Piersol (2011). *Random data: Analysis and measurement procedures* (3rd ed.). John Wiley & Sons.

Blanckaert, K. and U. Lemmin (2006). Means of noise reduction in acoustic turbulence measurements. *Journal of Hydraulic Research 44*(1), 3–17.

Bluteau, C. E., N. L. Jones, and G. N. Ivey (2011). Estimating turbulent kinetic energy dissipation using the inertial subrange method in environmental flows. *Limnol. Oceanogr.: Methods 9*(7), 302–321.

Chen, C.-T. A. and F. J. Millero (1986). Thermodynamic properties for natural waters covering only the limnological range. *Limnology and Oceanography 31*(3), 657–662.

Cole, J. J., Y. T. Prairie, N. F. Caraco, W. H. McDowell, L. J. Tranvik, R. G. Striegl, C. M. Duarte, P. Kortelainen, J. A. Downing, J. J. Middelburg, et al. (2007). Plumbing the global carbon cycle: integrating inland waters into the terrestrial carbon budget. *Ecosystems 10*(1), 172–185.

Czikowsky, M. J., S. MacIntyre, E. W. Tedford, J. Vidal, and S. D. Miller (2018). Effects of wind and buoyancy on carbon dioxide distribution and air-water flux of a stratified temperate lake. *Journal of Geophysical Research: Biogeosciences 123*(8), 2305–2322.

Dillon, T., J. Richman, C. Hansen, and M. Pearson (1981). Near-surface turbulence measurements in a lake. *Nature* (290), 390–392.

Doroudian, B., F. Bagherimiyab, and U. Lemmin (2010). Improving the accuracy of four-receiver acoustic Doppler velocimeter (ADV) measurements in turbulent boundary layer flows. *Limnology and Oceanography: Methods 8*(11), 575–591.

Downing, J. A., Y. Prairie, J. Cole, C. Duarte, L. Tranvik, R. G. Striegl, W. McDowell, P. Kortelainen, N. Caraco, J. Melack, et al. (2006). The global abundance and size distribution of lakes, ponds, and impoundments. *Limnology and Oceanography 51*(5), 2388–2397.

Durgesh, V., J. Thomson, M. C. Richmond, and B. L. Polagye (2014). Noise correction of turbulent spectra obtained from acoustic Doppler velocimeters. *Flow Measurement and Instrumentation 37*, 29–41.

Erkkilä, K.-M. (2015). Comparison of measurements and water boundary layer model for methane and carbon dioxide fluxes over a boreal lake. Master's thesis, University of Helsinki.

Erkkilä, K.-M., A. Ojala, D. Bastviken, T. Biermann, J. J. Heiskanen, A. Lindroth, O. Peltola, M. Rantakari, T. Vesala, and I. Mammarella (2018). Methane and carbon dioxide fluxes over a lake: comparison between eddy covariance, floating chambers and boundary layer method. *Biogeosciences 15*(2), 429–445.

Heiskanen, J. J., I. Mammarella, S. Haapanala, J. Pumpanen, T. Vesala, S. MacIntyre, and A. Ojala (2014). Effects of cooling and internal wave motions on gas transfer coefficients in a boreal lake. *Tellus B 66*.

Heiskanen, J. J., I. Mammarella, A. Ojala, V. Stepanenko, K.-M. Erkkilä, H. Miettinen, H. Sandström, W. Eugster, M. Leppäranta, H. Järvinen, et al. (2015). Effects of water clarity on lake stratification and lake-atmosphere heat exchange. *Journal of Geophysical Research: Atmospheres 120*(15), 7412–7428.

Hsieh, C.-I. and G. G. Katul (1997). Dissipation methods, Taylor's hypothesis, and stability correction functions in the atmospheric surface layer. *Journal of Geophysical Research: Atmospheres 102*(D14), 16391–16405.

Hurther, D. and U. Lemmin (2001). A correction method for turbulence measurements with a 3D acoustic Doppler velocity profiler. *Journal of Atmospheric and Oceanic Technology 18*(3), 446–458.

Imberger, J. (1985). The diurnal mixed layer. *Limnology and Oceanography 30*(4), 737–770.

Kaimal, J. C. and J. J. Finnigan (1994). *Atmospheric boundary layer flows: Their structure and measurement*. Oxford University Press.

Kestin, J., M. Sokolov, and W. A. Wakeham (1978). Viscosity of liquid water in the range 8 °C to 150 °C. *Journal of Physical and Chemical Reference Data 7*(3), 941–948.

Kocsis, O., H. Prandke, A. Stips, A. Simon, and A. Wüest (1999). Comparison of dissipation of turbulent kinetic energy determined from shear and temperature microstructure. *Journal of Marine Systems 21*(1), 67–84.

Lhermitte, R. and R. Serafin (1984). Pulse-to-pulse coherent Doppler sonar signal processing techniques. *Journal of Atmospheric and Oceanic Technology 1*(4), 293–308.

Lombardo, C. and M. Gregg (1989). Similarity scaling of viscous and thermal dissipation in a convecting surface boundary layer. *Journal of Geophysical Research: Oceans 94*(C5), 6273–6284.

Lorke, A., D. F. McGinnis, and A. Maeck (2013). Eddy-correlation measurements of benthic fluxes under complex flow conditions: Effects of coordinate transformations and averaging time scales. *Limnology and Oceanography: Methods 11*(8), 425–437.

Maanmittauslaitos (2018). Karttapaikka. `https://asiointi.maanmittauslaitos.fi/karttapaikka/`. Accessed on Oct 12th, 2018.

MacIntyre, S., A. T. Crowe, A. Cortés, and L. Arneborg (2018). Turbulence in a small arctic pond. *Limnology and Oceanography*.

Mammarella, I., A. Nordbo, Ü. Rannik, S. Haapanala, J. Levula, H. Laakso, A. Ojala, O. Peltola, J. Heiskanen, J. Pumpanen, et al. (2015). Carbon dioxide and energy fluxes over a small boreal lake in southern finland. *Journal of Geophysical Research: Biogeosciences 120*(7), 1296–1314.

Nortek AS (2004). *Vectrino velocimeter: User guide, Rev. C*. Nortek AS.

O'Reilly, C. M., S. Sharma, D. K. Gray, S. E. Hampton, J. S. Read, R. J. Rowley, P. Schneider, J. D. Lenters, P. B. McIntyre, B. M. Kraemer, et al. (2015). Rapid and highly variable warming of lake surface waters around the globe. *Geophysical Research Letters 42*(24).

Sander, J., A. Simon, T. Jonas, and A. Wüest (2000). Surface turbulence in natural waters: A comparison of large eddy simulations with microstructure observations. *Journal of Geophysical Research: Oceans 105*(C1), 1195–1207.

Sellar, B., S. Harding, and M. Richmond (2015). High-resolution velocimetry in energetic tidal currents using a convergent-beam acoustic Doppler profiler. *Measurement Science and Technology 26*(8), 085801.

Sunderland, P. and W. K. Melville (2015). Measuring turbulent kinetic energy dissipation at a wavy sea surface. *Journal of Atmospheric and Oceanic Technology 32*(8), 1498–1514.

Tedford, E. W., S. MacIntyre, S. D. Miller, and M. J. Czikowsky (2014). Similarity scaling of turbulence in a temperate lake during fall cooling. *Journal of Geophysical Research: Oceans 119*(8), 4689–4713.

Tennekes, H. and J. L. Lumley (1972). *A first course in turbulence*. MIT Press.

Thorpe, S. A. (2007). *An introduction to ocean turbulence*. Cambridge University Press.

Tikkanen, M. (2002). Long-term changes in lake and river systems in Finland. *Fennia-International Journal of Geography 180*(1-2), 31–42.